



# Size effects in underwater granular collapses: Experiments and coupled lattice Boltzmann and discrete element method simulations

G. C. Yang 

*School of Aeronautics and Astronautics, Sun Yat-sen University, Guangzhou 510275, China  
and Department of Civil Engineering, The University of Hong Kong,  
Haking Wong Building, Pokfulam Road, Hong Kong*

L. Jing \* and C. Y. Kwok †

*Department of Civil Engineering, The University of Hong Kong, Haking Wong Building,  
Pokfulam Road, Hong Kong*

Y. D. Sobral 

*Departamento de Matemática, Universidade de Brasília, Campus Universitário Darcy Ribeiro,  
70910-900 Brasília, DF, Brazil*



(Received 30 July 2020; accepted 4 October 2021; published 3 November 2021)

Immersed granular collapse is a common model case for the study of transient geophysical flows. This paper examines the effects of column size on granular collapses in water, with an emphasis on the granular flow mobility. Laboratory-scale experiments of underwater granular collapses with three different column sizes are carried out, together with their numerical simulations using the coupled lattice Boltzmann and discrete element method. Both experimental and numerical data show that, for an identical aspect ratio, a larger underwater granular collapse results in higher flow mobility and a longer runout distance normalized by the initial column length  $L_i$  (increased by 18% on average as  $L_i$  increases from 3 to 10 cm). Simulations show that as the column size increases, there is more potential energy being transferred into the kinetic energies of the fluid and the particles, and there is a positive relationship between the column size and the efficiency of energy conversion of the particle kinetic energies from vertical to horizontal directions, which contributes to a higher underwater granular flow mobility in larger cases. The reason is twofold. First, the fluid inertia scales disproportionately with the column size. A stronger eddy with high inertia is induced in the large case, which penetrates through the flowing layer of the granular phase and pushes the particles forward to reach a longer runout distance. Second, large underwater granular collapses are accompanied with more significant contact lubrication, which promotes basal slip and dissipates less energy during horizontal spreading.

DOI: [10.1103/PhysRevFluids.6.114302](https://doi.org/10.1103/PhysRevFluids.6.114302)

## I. INTRODUCTION

Large-scale geophysical flow is a ubiquitous phenomenon in nature that plays a crucial role in shaping the landscape and sometimes brings enormous losses to human life and property. Such mass

\*Now at Department of Chemical and Biological Engineering, Northwestern University, Evanston, Illinois 60208, USA.

†[fkwok8@hku.hk](mailto:fkwok8@hku.hk)

movements are usually composed of granular materials (soils and rocks) surrounded by an ambient fluid. Despite the continued interest in such extreme natural events in the engineering and scientific fields, a unified theoretical description of unsteady granular flow behaviors still remains a challenge [1–3], especially when the complex interactions between the granular materials and the ambient fluid cannot be ignored [4]. One primary issue is the prediction of runout distance of geophysical flows for the purpose of hazard mitigation.

Collapse of granular columns on a horizontal bottom plane has received much attention in recent years for the study of unsteady granular flows characterized by a transition between static and flowing states. The dynamics of granular collapses is further complicated by the coexistence of static and flowing regions within the column during the flow. In dry granular collapses, where the interstitial fluid (air) plays a negligible role [5,6], the collapse dynamics is mainly controlled by the initial aspect ratio ( $a$ ) of the granular columns [7–10]. When the aspect ratio is small, the granular column collapses along a sliding plane that intersects the top surface of the column, resulting in a trapezoidal final deposit. As the aspect ratio increases, the vertical acceleration becomes more predominant and severe collisions take place when particles impact on the stagnant materials at the bottom [11]. The final deposit turns into a triangular shape. In addition, piecewise power law relationships have been proposed to relate the final runout distance  $L_f$  and the residual column height  $H_f$  to the initial aspect ratio [7–10].

Unlike the dry scenario in which the granular inertia dominates, the interstitial fluid has significant inertial and viscous effects on the motion of particles in immersed granular collapses [5,6]. Thompson and Huppert [12] first carried out granular collapse experiments in water. It was found that the particles close to the granular free surface are eroded by the surrounding water, forming a current that transports forward and deposits farther than particles would do when traveling in air. The erosion of particles by water has been associated with the energy conversion from vertical to horizontal direction that determines the overall flow mobility in our recent numerical study [11]. However, if the fluid viscosity increases, the presence of fluid can significantly hinder the particle motion caused by the enhanced viscous drag acting on the particles [6,13,14]. The dynamics of immersed granular collapse is also heavily dependent on the initial solid volume fraction [15–18]. A granular column initially at a loose state collapses faster and propagates farther compared to the same granular collapse but with a dense packing. It is because of the negative and positive excess pore fluid pressures induced by the dilation and contraction of the granular column, respectively, that enhance and weaken the frictional resistance of granular materials, thereby affecting the granular flow mobility [17–19]. There are other factors that can affect the dynamics of granular collapses, including the grain size [20] and the presence of a fluid-air interface [21,22].

In the study of geophysical flows, one striking issue is the increase of flow mobility (or the reduction of apparent friction) with the increase of the total volume of the flow. Different theories have been proposed to explain this volume-induced lubrication, for instance, local melting near the gliding surface due to high energy concentration [23], acoustic fluidization caused by strong acoustic waves [24], lubrication by a layer of trapped and compressed air [25,26], and hydroplaning due to a pressurized layer of water in a submarine environment [27]. Early granular collapse experiments in air showed that the final runout distance  $L_f$  normalized by the initial column length  $L_i$  is nearly independent on the column size, within the limits of experimental error [7,8]. However, a more recent study has demonstrated a clear increase of normalized runout distance with the increasing column size, benefiting from the improved accuracy of experimental measurements by using three-dimensional laser scanning [28]. In experiments of steady granular flows down rough inclined slopes, a similar granular behavior of strength weakening as the flow thickness increases was observed [29].

The current study is inspired by this size-dependent granular flow mobility problem with the objective of uncovering the role of column size in underwater granular collapses, which has not been discussed in the literature thoroughly. We perform underwater granular collapse experiments with different column sizes, considering a range of small initial aspect ratios ( $a \leq 2$ ) to avoid nontrivial effects of free-fall dynamics at higher aspect ratios [11]. While experimental observations can

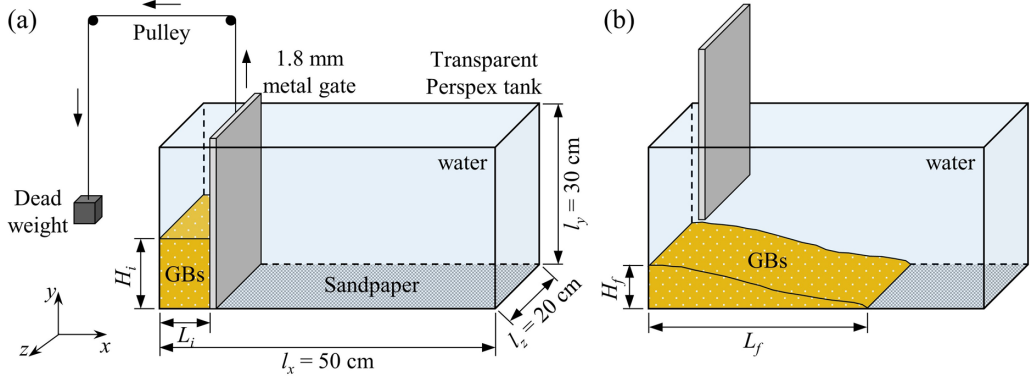


FIG. 1. Sketch of the experimental setup for underwater collapses of granular columns composed of glass beads (GBs): (a) initial condition, (b) final deposit.

provide solid evidence that supports phenomenological explanations, they offer limited information about the internal flow structure that is essential to understand the micromechanics of the granular collapse, which suggests the need for accurate numerical simulations. There are mainly two successful ways of modeling immersed granular collapse problems. First, constitutive models governing the behaviors of fluid-particle mixtures can be developed within a continuum framework, such as the mixture theory [30]. The hydrodynamic equations are then solved by a numerical method, which is usually an approach that allows large deformations [16,31,32]. The second method is to couple two different solvers for particle mechanics and fluid dynamics [11,13,17,33]. Considering the fact that the size effects in granular collapses could originate from particle-scale interactions, we here simulate underwater granular collapses by coupling the discrete element method (DEM) and the lattice Boltzmann method (LBM), which can fully resolve the complex fluid-particle and interparticle interactions without relying on *ad hoc* constitutive laws [18,33].

This paper is organized as follows. The experimental setup and measurements are presented in Sec. II. The LBM-DEM formulation is briefly introduced in Sec. III, together with the numerical configuration for granular collapse simulations. Section IV provides the experimental and numerical evidence for the column size effects on the macroscopic collapse dynamics, with an emphasis on the granular flow mobility. Section V discusses the underlying mechanisms of column size effects. Conclusions are drawn in Sec. VI.

## II. LABORATORY EXPERIMENTS

### A. Apparatus and material properties

Figure 1(a) presents the experimental setup for the granular collapses in water. It consists of a transparent Perspex tank with dimensions 50, 30 and 20 cm in the  $x$ ,  $y$ , and  $z$  directions, respectively. An 80 Cw grit-size sandpaper is glued to the bottom wall to make the base rough. A vertically positioned 1.8-mm-thick aluminum gate (facing the  $x$ -direction) is constrained by a pair of slots on the side walls, forming a reservoir behind the gate for constructing the granular columns with the initial length and height denoted by  $L_i$  and  $H_i$ , respectively. There are three pairs of slots on the side walls at different locations, so that we can have a variable  $L_i = 3, 5$ , and 10 cm. The gate is connected to a pulley system, which can be used to rapidly lift the gate up by releasing the dead weight to mimic a dam-break scenario. The application of the pulley system enables the gate to be removed steadily (so that the disturbance to the granular column and the fluid field is reduced compared to gate removal by hand) and consistently across different tests. We have verified that the time of gate removal remains small compared to the whole flow duration from initiation to deposition. The final deposit of granular collapse is sketched in Fig. 1(b). The final runout distance and the residual height of the particles are denoted by  $L_f$  and  $H_f$ , respectively.

The particles used in this study are glass beads. To determine the particle size distribution (PSD) of the glass beads, QICPIC analysis (based on digital image processing on two dimensional projections of particles in a fast moving air stream) is carried out with three individual batches of samples. The three obtained PSD curves almost overlap with each other, showing consistent statistics. The particle diameter is measured to be  $d_p = 1.44 \pm 0.2$  mm. Also, the glass beads are quite spherical with a sphericity of 0.94. The particle density is measured to be  $2468 \text{ kg/m}^3$ . To characterize the frictional property of the glass beads, they are gently poured onto a cylindrical rough base, resulting in a maximum slope (i.e., the angle of repose) of  $21.3^\circ$ . For the immersed granular collapses, the glass beads are immersed in water at room temperature, and we consider the water density and viscosity to be  $\rho_f = 1000 \text{ kg/m}^3$  and  $\mu_f = 0.001 \text{ Pa s}$ , respectively.

### B. Test procedures

The experimental procedures are as follows. After filling the tank with water to a high enough level, the metal gate is placed at a desired position such that granular columns with different initial lengths can be created. The total dry mass of glass beads used in each test is first estimated based on a presumed initial packing density (i.e., 0.62) and the target column size. The total mass is later used for calculating the actual initial packing density. The glass beads are then gently poured into the reservoir enclosed by the gate and the tank walls. In immersed granular collapses, the trapped air bubbles between the particles may influence the collapse dynamics and the flow mobility due to capillary effects [34]. Therefore, in our experiments, the glass beads are stirred vigorously by a propeller driven by an electronic motor. Once the stirring process stops, all glass beads settle down quickly within a few seconds. As a result, a relatively loose packing is obtained. After that, the top surface of the granular column is carefully flattened using a spatula with a minimum amount of compaction.

The packing density is strictly controlled in our experiments by tapping the side walls continuously to adjust the height (and hence the volume) of the granular column to a target value. The top surface of the granular columns remains flat during tapping. The resulting packing density averaged among all test cases is  $0.621 \pm 0.013$ . Note that the influences of packing density on immersed granular collapses have been investigated previously [15,17,18], which is expected to be less dominant in this study due to the relatively large particle size and small fluid viscosity. Once the granular column and the fluid in the reservoir are quiescent, the metal gate is lifted up rapidly by releasing the dead weight [see Fig. 1(a)]. Due to the friction of the gate, the glass beads at the leading edge of the granular column in contact with the gate gain an initial upward motion. Once the gate is removed, the granular column collapses onto the horizontal bottom plane and the grains propagate forward in the  $x$ -direction.

Experiments of underwater granular collapses with the initial lengths  $L_i = 3$  cm (S: small case),  $L_i = 5$  cm (M: medium case), and  $L_i = 10$  cm (L: large case) are conducted. The aspect ratios ( $a = H_i/L_i$ ) tested are 0.5, 0.65, 0.8, 1, 1.5, and 2. Experiments with  $a = 0.3$  are carried out when  $L_i = 5$  and 10 cm, and another experiment with  $a = 0.2$  is performed when  $L_i = 10$  cm. In total, there are 21 sets of experiments, each of which is carried out twice to ensure repeatability.

### C. Data acquisition and postprocessing

The glass beads are illuminated by an LED lamp. In the experiments, we ignore the small variations of the measured properties in the spanwise ( $z$ ) direction and consider that the granular collapse is essentially two-dimensional. That means we can mainly focus on the collapse dynamics from a side view. A camera is carefully aligned in the horizontal direction and records the whole granular collapse with a resolution of 3840 by 2160 pixels at 60 frames per second. To correct the perspective error of the images, a depth-correction algorithm is developed using OpenCV to transform the markers on the side wall into the four corners of a perfect rectangle. After that, the free surface of the glass beads during the collapse at each frame is extracted, which enables the

measurements of the instantaneous front position  $x_{ft}$  and column height, including the final values (i.e.,  $L_f$  and  $H_f$ ). For the range of column sizes tested in our experiments, the tank [see Fig. 1(a)] is large enough and there are no particles reaching the right wall in any of the test cases. Note that there could be outrunner particles in dry granular collapses, which causes difficulties in the determination of the front position [7–9], but this is less of a problem in immersed cases, except for some occasions where dispersed particles above the granular free surface are observed during propagation (see Sec. V D).

### III. NUMERICAL MODELING

#### A. LBM-DEM formulation

Over the past two decades, the lattice Boltzmann method (LBM) has become an alternative fluid solver to the traditional computational fluid dynamics (CFD). Our recent work applied LBM to study the effects of bed form roughness on sediment transport in a turbulent environment [35]. One popular approach to simulate a two-phase flow with particles traveling in a viscous fluid is coupling a fluid solver with the discrete element method (DEM), such as the CFD-DEM technique we used recently to study the effects of aspect ratio, particle size, and fluid viscosity on immersed granular collapses [11,14]. When CFD is coupled with DEM, a semiempirical drag model is required to calculate the hydrodynamic forces between the fluid and the particles [36]. Alternatively, we have also successfully coupled LBM with DEM, in which the complex fluid-particle interactions (both drag force and torque) are fully resolved based on the fundamental law of momentum conservation [18,33]. In this study, a coupled LBM-DEM method using an immersed moving boundary technique [37] is applied to simulate underwater granular collapses. Our LBM-DEM framework has been validated against multiple benchmark cases in [33], where a detailed mathematical formulation of LBM-DEM is also presented. In the following, only key equations are summarized.

In LBM, a three-dimensional lattice structure with discrete velocities pointing to 19 different directions (usually denoted as D3Q19) is adopted. The transport equation with a Bhatnagar-Gross-Krook approximation for the collision operator [38] is written as

$$f_i(\mathbf{x} + \mathbf{c}_i \delta_t, t + \delta_t) - f_i(\mathbf{x}, t) = -\frac{1}{\tau} [f_i(\mathbf{x}, t) - f_i^{\text{eq}}(\mathbf{x}, t)], \quad (1)$$

where  $f_i$  is the density distribution function that is related to the number of fluid particles at time  $t$  positioned at  $\mathbf{x}$  and moving with velocity  $\mathbf{c}_i$  along the  $i$ th direction at each lattice node. The time step and the relaxation time are denoted as  $\delta_t$  and  $\tau$ , respectively. The relaxation time physically determines how fast the current density distribution function recovers the equilibrium state depending on the local fluid density and velocity (the Maxwell-Boltzmann distribution) [39].

According to the conservation of mass and momentum, the macroscopic fluid density  $\rho_f$  and velocity  $\mathbf{u}_f$  can be reconstructed from the velocity moments of the density distribution functions:

$$\rho_f = \sum_{i=0}^{18} f_i, \quad (2)$$

$$\rho_f \mathbf{u}_f = \sum_{i=0}^{18} \mathbf{c}_i f_i. \quad (3)$$

From the Chapman-Enskog expansion, the fluid viscosity  $\nu_f$  can be related to the relaxation time  $\tau$ , the lattice spacing  $\delta_x$ , and the LBM time step  $\delta_t$  as [40]

$$\nu_f = c_s^2 \left( \tau - \frac{1}{2} \right) \frac{\delta_x^2}{\delta_t}, \quad (4)$$

where  $c_s$  is the speed of sound and is equal to  $1/\sqrt{3}$  in lattice units for the D3Q19 lattice arrangement.

While LBM is applied to solve the fluid dynamics, DEM is adopted to resolve the particle mechanics [41]. The interparticle collision is solved by a simplified Hertz contact model [42], which takes several measurable material properties as inputs, including Young's modulus, Poisson's ratio, coefficients of restitution and friction, and particle size. Details of the contact model is available in Appendix C of Ref. [14].

The coupling between the fluid and the solid particles is achieved via the immersed moving boundary method [37]. The fundamental principle is to introduce a new collision operator that depends on the solid coverage ratio  $\varepsilon$  of a specific lattice cell:

$$f_i(\mathbf{x} + \mathbf{c}_i \delta_t, t + \delta_t) - f_i(\mathbf{x}, t) = -\frac{1}{\tau}(1 - B)[f_i(\mathbf{x}, t) - f_i^{\text{eq}}(\mathbf{x}, t)] + B\Omega_i^s, \quad (5)$$

where  $B$  is a weighting function of  $\varepsilon$  and  $\tau$  that defines the relative importance of each of the phases for every lattice cell [37]:

$$B(\varepsilon, \tau) = \frac{\varepsilon(\tau - 1/2)}{(1 - \varepsilon) + (\tau - 1/2)}. \quad (6)$$

When a lattice cell is fully covered by a solid particle (i.e.,  $\varepsilon = 1$ ), the right-hand side of Eq. (5) recovers the solid collision operator,  $\Omega_i^s$ . In the current LBM-DEM formulation,  $\Omega_i^s$  is written based on the nonequilibrium bounce-back scheme to ensure the no-slip boundary condition between fluid and solid [43]:

$$\Omega_i^s = f_{-i}(\mathbf{x}, t) - f_{-i}^{\text{eq}}(\rho_f, \mathbf{u}_f) + f_i^{\text{eq}}(\rho_f, \mathbf{u}_s) - f_i(\mathbf{x}, t), \quad (7)$$

where  $\mathbf{u}_s$  denotes the macroscopic solid particle velocity at the position of the lattice node  $\mathbf{x}$ . The subscript  $-i$  denotes the opposite direction of  $i$ .

The introduction of  $B\Omega_i^s$  on the right-hand side of Eq. (5) represents the change of momentum due to the presence of solid particles. If the  $k$ th particle covers  $N_{sc}$  lattice cells with  $\varepsilon > 0$ , the hydrodynamic force  $\mathbf{F}_k^f$  on this particle can be calculated by adding together the momentum transfer along all 19 directions at all covered lattice cells:

$$\mathbf{F}_k^f = \sum_{j=1}^{N_{sc}} B_j \sum_{i=0}^{18} \Omega_i^s \mathbf{c}_i. \quad (8)$$

The hydrodynamic torque  $\mathbf{T}_k^f$  is the cross product of the force and the corresponding lever arm, which gives

$$\mathbf{T}_k^f = \sum_{j=1}^{N_{sc}} \left[ B_j (\mathbf{x}_j - \mathbf{x}_k) \times \sum_{i=0}^{18} \Omega_i^s \mathbf{c}_i \right], \quad (9)$$

where  $\mathbf{x}_k$  is the center of mass of the  $k$ th particle and  $\mathbf{x}_j$  denotes the coordinates of the center of the  $j$ th lattice cell that is fully or partially covered by the particle. The hydrodynamic force and torque calculated from Eqs. (8) and (9) are added to the contact forces for the update of particle velocities and positions according to Newton's second law [33].

## B. Numerical configuration

The coupled LBM-DEM model is applied to simulate the underwater granular collapse experiments presented in Sec. II. In addition, to further clarify the role of interstitial fluid in the column size effects on underwater granular collapses, dry granular collapses with different column sizes when  $a = 1$  are simulated using only the DEM solver for comparison. The particle size distribution (PSD) in simulations follows a Gaussian distribution with mean and standard deviation equal to  $d_p$  and  $0.1d_p$ , respectively. The resulting PSD agrees with that of glass beads in our experiments very well (see Ref. [44] for more details). The granular columns in simulations are constructed by



means of gravitational deposition inside a reservoir delimited by a “virtual” gate. Unlike laboratory experiments, the virtual gate can be deleted to initiate granular column collapses without any gate removal effects (see Sec. II B). A layer of particles with a uniform size 1 mm was fixed at the bottom, following the simple cubic packing, to mimic the rough base [45].

The particles in simulations have the same density as the glass beads in our experiments ( $2468 \text{ kg/m}^3$ ). For particle-particle and particle-wall interactions, Young’s modulus and Poisson’s ratio are defined as  $2.5 \times 10^8 \text{ Pa}$  and 0.24, respectively. Note that a reduced Young’s modulus compared to glass beads is adopted so that the DEM simulation can be stable at a larger time step. Our previous study has shown that reducing Young’s modulus to this extent has little effect on the collapse dynamics, but improves computational efficiency significantly [14]. To generate relatively dense granular columns, the friction coefficient is set to be zero during sample preparation. As a result, all granular columns in our simulations have an average solid volume fraction equal to 0.62, which is very close to the value measured in our experiments. To stabilize the system quickly, the coefficient of restitution is set to be zero during the sample preparation stage. Before releasing the granular columns, the friction coefficient is set to be 0.4 and the coefficient of restitution is set to be 0.65, both of which are set according to the property of glass beads. The fluid in simulations has the same material properties as water with the density  $\rho_f = 1000 \text{ kg/m}^3$  and the viscosity  $\mu_f = 0.001 \text{ Pa s}$ .

The simulation domain varies with the column geometry in  $x$  and  $y$  directions, with a minimum size of  $l_x = 2.8H_i$  and  $l_y = 1.4H_i$ . The length in the  $z$ -direction is fixed to be  $l_z = 15 \text{ mm}$  (more than 10 particle diameters) for all cases. Periodic boundary conditions are defined for both the solid and fluid phases in the  $z$ -direction. Solid walls with the same properties as particles are placed at other boundaries for the solid phase. The top fluid boundary is defined as free-slip and all the other fluid boundaries are defined as no-slip. It has been verified that any increase in the simulation domain (including dimensions in  $x$ ,  $y$  and  $z$  directions) has little influence on the granular collapse dynamics.

In LBM, the lattice spacing is set so that there are 15 lattice cells across one  $d_p$ , i.e.,  $\delta_x = d_p/15 = 0.096 \text{ mm}$ . The relaxation time is defined as  $\tau = 0.506$ . Rearranging Eq. (4) gives the LBM time step  $\delta_t = 1.8432 \times 10^{-5} \text{ s}$ . The DEM time step ( $\Delta t$ ) for a stable simulation is smaller than the LBM time step  $\delta_t$ . Therefore, to synchronize the LBM and DEM simulations, a subcycling scheme is adopted such that 100 DEM cycles are performed for each LBM time step [33]. As a result, the DEM time step is  $\Delta t = \delta_t/100 = 1.8432 \times 10^{-7} \text{ s}$ . Note that the hydrodynamic forces and torques remain unchanged during subcycling. To validate our LBM-DEM model and the selected input parameters, a one-to-one comparison between the numerical results and the measured experimental data is carried out in Sec. IV A.

Consistent with the experiments, numerical simulations of underwater granular collapses with  $L_i = 3 \text{ cm}$ ,  $5 \text{ cm}$ ,  $10 \text{ cm}$  and with  $a$  ranging from 0.5 to 2 are performed. To save computational time, each case of LBM-DEM simulations is conducted only once for the main numerical results presented in this study. In the Appendix, a simulation with  $L_i = 5 \text{ cm}$  and  $a = 1$  is repeated for five times with different random seeds, and we show that the effect of random seed is negligible when compared to the column size effects, confirming the repeatability of our numerical simulations. The LBM-DEM simulations are carried out on the HPC2015 platform at the University of Hong Kong. All cases are simulated with six compute nodes, each of which is equipped with two 10-core Intel Xeon E5-2600 v3 processors and 96 GB physical memory. In general, the simulation time scales with the domain size. Taking the case with  $L_i = 10 \text{ cm}$  and  $a = 1$  as an example, the simulation involves 58 809 particles and takes about 8 days to finish.

#### IV. EXPERIMENTAL AND NUMERICAL RESULTS

This section presents the phenomenological description of the column size effects on underwater granular collapses, with a particular emphasis on the granular flow mobility. The analysis is mainly based on direct experimental and numerical observations of the runout distance, the residual column

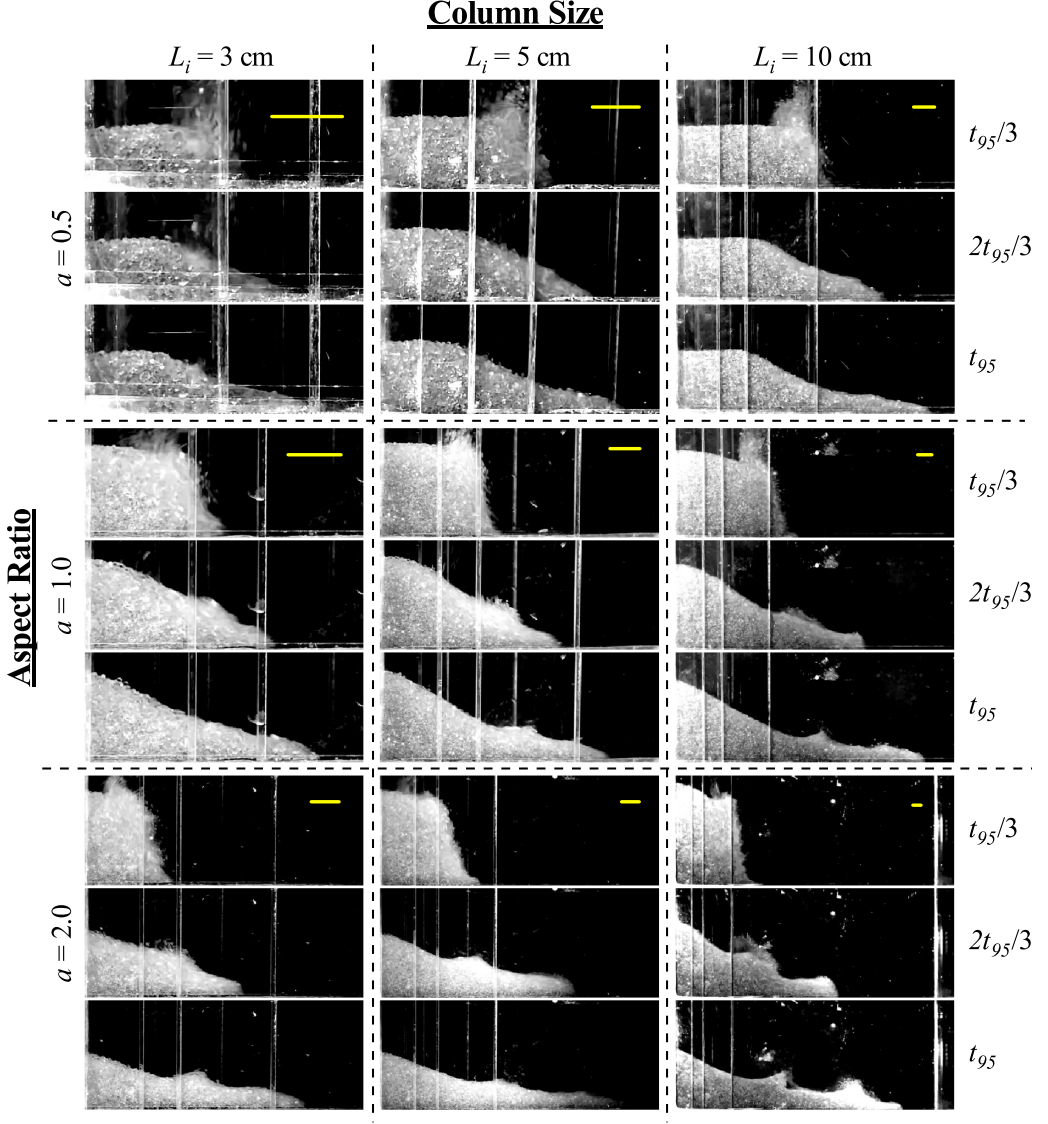


FIG. 2. Underwater granular collapses in experiments. The three columns and rows correspond to three different column sizes (small, medium, and large) and aspect ratios ( $a = 0.5, 1, 2$ ), respectively. Snapshots at three time instants,  $t_{95}/3$ ,  $t_{95}/2$ , and  $t_{95}$ , for each case are shown. The yellow bars are the scales indicating a fixed length equal to 1.5 cm. Examples of video recordings of underwater granular collapses with small, medium, and large sizes are available in the Supplemental Material [47].

height and the flow duration. As for the center of mass of the flowing particles that is difficult to measure in experiments, only numerical results are evoked and discussed.

#### A. Experimental observations and model validation

To visualize the effects of the column size in underwater granular collapses, snapshots of the small, medium and large granular columns with the aspect ratio  $a = 0.5, 1$ , and  $2$  during the collapses are presented in Fig. 2. For each case, three snapshots are extracted at three typical



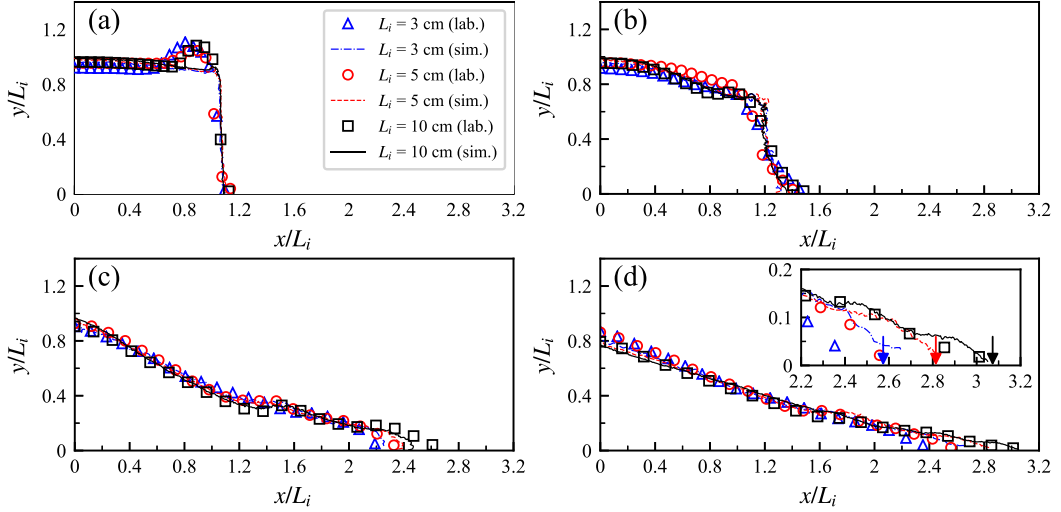


FIG. 3. Direct comparison between the numerical results (sim.) and the experimental data (lab.) for the time evolution of granular free surface from granular collapses with different column sizes when  $a = 1$ . The free surface of the granular phase at four time instants  $t = t_c, 2t_c, 5t_c$ , and  $10t_c$  has been extracted and compared from (a) to (d). The inset of (d) zooms in the frontal region of the final deposit with the arrows pointing to the front positions averaged among five measurements in experiments.

time instants  $t = t_{95}/3, 2t_{95}/3$  and  $t_{95}$ , where  $t_{95}$  is the time instant corresponding to 95% of the normalized final runout distance  $(L_f - L_i)/L_i$  (see Sec. IV B).

During underwater granular collapses, it is the movement of particles that sets the surrounding water into motion via hydrodynamic interactions. The water flow in turn exerts a drag force on the particles as a feedback. When both the column size and the aspect ratio are small, i.e., the top-left corner of Fig. 2, there is a small grain inertia developed during the collapse. A weak eddy is induced in the fluid field, which can barely alter the particle motion. In this case, the surrounding water mainly poses a resisting force on the particles in the form of viscous drag. Also, the surface of the final deposit appears to be quite smooth.

However, as the column size and the aspect ratio increase, the particles can gain a much higher kinetic energy during the collapse, and their faster motion induces a much stronger eddy that carries higher fluid inertia. The high-intensity eddy is powerful enough to erode the particles close to the granular free surface and put them into suspension (see the case with  $L_i = 10$  cm and  $a = 2$  in Fig. 2). This phenomenon has been reported in previous CFD-DEM simulations with aspect ratios of 4 and higher [11]. Our experimental data show that the erosion of granular free surface can also take place at a smaller aspect ratio as long as the column size is large enough. When the fluid energy is gradually dissipated due to the viscous effect, the suspended particles settle down slowly, forming a wavy surface of the final deposit. The complex fluid-particle interactions have a great influence on the flow mobility. A more quantitative analysis is presented in Sec. V based on the numerical results.

The cases with  $a = 1$  but different column sizes are taken as typical examples to validate our LBM-DEM model. Figure 3 directly compares the numerical results to the measured experimental data regarding the temporal evolution of the granular free surface. The experimental data for the granular free surface are averaged among two repeated tests to make the results more representative. The dimensions of the free surfaces are normalized by  $L_i$  and the time is scaled by  $t_c = \sqrt{H_i/g'}$ , where  $g' = g(\rho_p - \rho_f)/\rho_p$  is the reduced gravitational acceleration with  $g = 9.81$  m/s<sup>2</sup>.

When  $t = t_c$ , the particle displacements are small and the granular columns remain in a fairly rectangular shape, as shown in Fig. 3(a). The free surfaces suddenly rise up close to the top-right

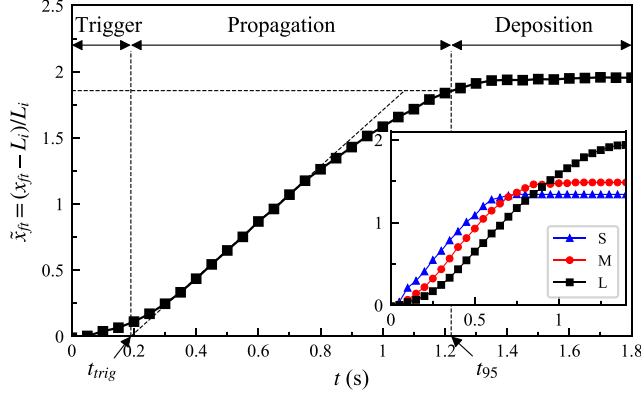


FIG. 4. Experimental results of the normalized front position  $\tilde{x}_{ft}$  plotted against time  $t$  when  $a = 1$  for the large case with  $L_i = 10$  cm. The inset compares the runout evolution between the small (S), medium (M), and large (L) cases.

corners of the granular columns for the experimental data, which is caused by the up-lifting of the gate. However, these bulges have little influence on the granular free surface at later stages of the flows. Figure 3 shows that the overall collapse sequence is rather similar across difference sizes after normalization. The major difference occurs at the frontal region. The inset of Fig. 3(d) plots the free surface profiles at the front when  $t = 10t_c$  (the moment all particles almost stop moving). Both the numerical results and the experimental data show that the deposit length increases with the column size. However, the experimental granular free surface profiles are consistently shorter than those in numerical simulations. It is probably due to the effect of side wall friction in experiments, such that the front position is slightly farther at the center (in the  $z$ -direction) and gradually reduces as moving towards the side walls. To alleviate the side wall effect, five measurements of the frontal position at uniformly distributed points across the  $z$ -direction have been carried out in each test and the averaged values are indicated by the arrows in the inset of Fig. 3(d). The averaged front positions in experiments are much closer to the values from numerical simulations, where periodic boundary conditions have been applied in the  $z$ -direction. All in all, the LBM-DEM simulations are in excellent agreement with the experiments in terms of the granular free surface evolution.

### B. Column size effects on runout

The front position normalized by the initial column length,  $\tilde{x}_{ft} = (x_{ft} - L_i)/L_i$ , is plotted against time in Fig. 4 for  $a = 1$ . The large case with  $L_i = 10$  cm is first shown for a typical description of the collapse sequence, which can be divided into three stages: triggering, propagation, and deposition. The following approach has been applied consistently throughout all experimental cases to delimit the three stages. A straight line is drawn through the points characterizing the period with a nearly constant propagation velocity. This straight line intercepts the horizontal axis at  $t_{trig}$ , which separates the triggering and propagation stages. Another time instant ( $t_{95}$ ) is used to delimit the propagation and deposition stages, when 95% of the normalized final runout distance is reached.

The inset of Fig. 4 compares the runout evolution between underwater granular collapses with three different column sizes at  $a = 1$ . It is found that the triggering time  $t_{trig}$  increases as the column size increases, which is probably due to the enhanced frictional resistance by the induced negative excess pore pressure caused by the dilation of the dense granular column [15,17,18]. Furthermore, the negative excess pore pressure takes longer time to dissipate due to the longer drainage paths in the larger case. Interestingly, the final runout distance in the large case is significantly longer than that in the small case, indicating a size-dependent granular flow mobility. Note that the runout distance presented in these results has already been normalized by the column size ( $L_i$ ).

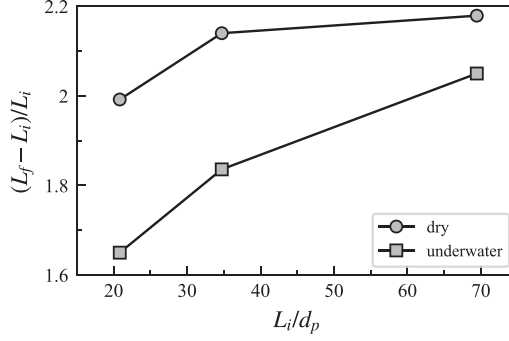


FIG. 5. Plot of the normalized final runout distance  $(L_f - L_i)/L_i$  against the normalized column size  $L_i/d_p$  for dry and underwater granular collapses.

As the effect of column size on the runout distance of underwater granular collapses is evident, it is interesting to investigate if similar effects exist in their dry counterparts. Figure 5 compares the dry and underwater granular collapses regarding the column size effects on the normalized final runout distance. For the range of column sizes considered in this study, the normalized runout distance is generally longer in the dry condition, because additional energy is dissipated through fluid-particle interactions in the underwater cases [11]. Nevertheless, the normalized runout distance increases at a faster rate in the underwater condition as the column size becomes larger, showing a more significant column size effect due to the presence of the interstitial fluid. It has also been demonstrated that the interstitial fluid is capable of enhancing the flow during the spreading stage [11,13]. Our result qualitatively agrees with a recent study on the size effects on the runout behavior of immersed granular collapses via two-dimensional numerical simulations [46]. According to Wang *et al.* [46], the runout distance of underwater granular collapses could exceed the value observed in the dry counterpart as long as the column size becomes large enough, despite the inhibiting effect of the fluid drag force.

### C. Scaling laws for runout and height

In the study of granular collapses, one of the most important previous findings is the scaling of normalized final runout distance  $\tilde{L}_f = (L_f - L_i)/L_i$  and the residual column height  $\tilde{H}_f = H_f/L_i$  with the initial aspect ratio  $a$ . To further show the influence of column size on the flow mobility, the measured experimental data ( $\tilde{L}_f$  and  $\tilde{H}_f$ ) are grouped according to the column size and plotted against  $a$  in Fig. 6. For the range of aspect ratios ( $a \leq 2$ ) considered in this study, there is a positive linear relationship between  $\tilde{L}_f$  and  $a$ , i.e.,  $\tilde{L}_f = \lambda a$  where  $\lambda$  is the coefficient of proportionality. This result agrees with a previous study on immersed granular collapses in fluids with different viscosities [6]. Linear fitting of the experimental and numerical data shows that the value of  $\lambda$  increases from 1.73 to 2.04 as the initial column length increases from 3 to 10 cm, and it has a strong linear correlation with the normalized column size  $L_i/d_p$  as

$$\lambda = 0.006 \frac{L_i}{d_p} + 1.63. \quad (10)$$

Immersed granular flows can be classified into three different regimes: grain inertial, fluid inertial, and viscous regimes [5]. According to Bougouin and Lacaze [6], the value of  $\lambda$  is bounded by the two limits 1.4 and 3.0 belonging to the viscous and grain inertial regimes, respectively. Figure 6(a) shows that our experimental and numerical data are well bounded by the two limits proposed by Bougouin and Lacaze [6]. Since the fluid used in our experiments is water and the particle-to-fluid density ratio is about 2.5 (which also remains constant as the column size changes),

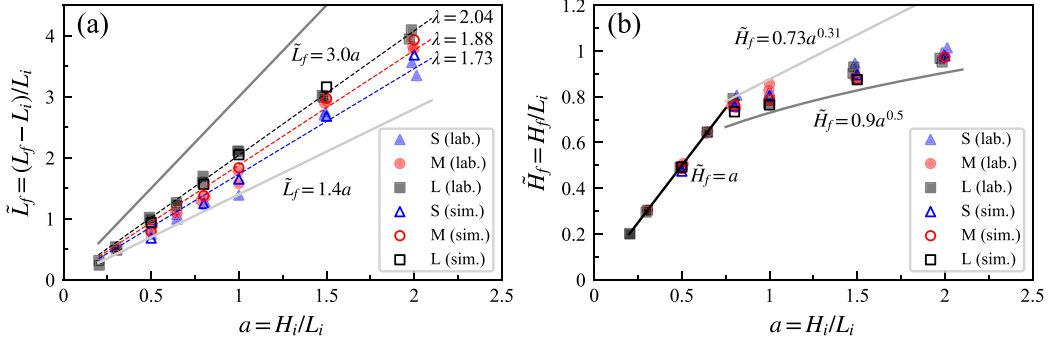


FIG. 6. (a) Plots of the normalized final runout distance  $(L_f - L_i)/L_i$  against the aspect ratio  $a$  for small, medium and large granular column collapses. The dashed lines are the linear fit of the experimental and numerical data with their color matching the data points. (b) Plots of the normalized residual column height  $H_f/L_i$  against the aspect ratio  $a$  for small, medium, and large granular column collapses. The dark gray and the light gray solid lines in (a) and (b) set the two limits characterized by the free-fall regime and the viscous regime, respectively, according to Bougouin and Lacaze [6].

the flow regime of the underwater granular collapses may belong to the fluid inertial and viscous regimes based on the phase diagram proposed by Courrech du Pont *et al.* [5]. Note that the specific value of  $\lambda$  in the fluid inertial regime was not reported in [6], but its value should lie slightly below the upper limit (i.e.,  $\lambda = 3.0$ ) of the grain inertial regime. Therefore, the increase of  $\lambda$  with  $L_i$  might be associated with the increase of fluid inertia as the column size increases, indicating a potential transition of flow regimes from viscous drag to inertia as the dominant mechanism governing the fluid-particle interactions in underwater granular collapses.

On the other hand, the column size has little influence on the scaling between the residual height  $\tilde{H}_f$  and the initial aspect ratio  $a$  [see Fig. 6(b)]. When  $a \leq 0.8$ , the morphology of the final deposit resembles a trapezoidal shape, meaning that the residual height  $H_f$  is roughly equal to the initial height  $H_i$ :  $\tilde{H}_f = H_f/L_i \approx H_i/L_i = a$ . When  $0.8 < a \leq 2$ , the final deposit turns to be triangular. The normalized residual height  $\tilde{H}_f$  still increases with  $a$ , but the increasing rate has been attenuated significantly. Note that further increase of  $a$  will cause reduction in  $\tilde{H}_f$  due to the erosion effect from the fluid eddies [6, 11]. The weak dependence of the normalized residual height  $\tilde{H}_f$  on the column size is probably due to the fact that  $\tilde{H}_f$  is mainly determined by the initial failure surface (inclined  $45^\circ + \phi/2$  to the horizontal direction based on the Mohr-Coulomb criterion, where  $\phi$  is the angle of friction). The initial failure surface is mainly a function of the material frictional strength, which is not affected by the column size and the collapse dynamics.

#### D. Runout duration

Another macroscopic variable that can be used to characterize granular collapses is the time duration of the propagation stage,  $t_{\text{run}} = t_{95} - t_{\text{trig}}$  (see Sec. IV B for the definitions of  $t_{95}$  and  $t_{\text{trig}}$ ). Figure 7(a) plots the runout duration  $t_{\text{run}}$  against the aspect ratio  $a$ . The dashed lines are the linear fitting of the experimental and numerical data from underwater granular collapses with different column sizes. It can be seen that the experimental and numerical data generally follow the same trend, further confirming the reliability of the pore-fluid resolved LBM-DEM model. The runout duration increases almost linearly as the aspect ratio increases. In addition, for the same aspect ratio, the runout duration is longer when the column size is larger.

We can collapse the data for runout duration by assuming a predominant free-fall over the height  $H_i$  and under the reduced gravity  $g' = g(\rho_p - \rho_f)/\rho_p$  due to the buoyancy effect, as suggested by Jing *et al.* [11]. The runout duration  $t_{\text{run}}$  is normalized by the characteristic time  $t_c = \sqrt{H_i/g'}$  and plotted against the aspect ratio  $a$  in Fig. 7(b). When  $a < 0.75$ , the experimental data does not

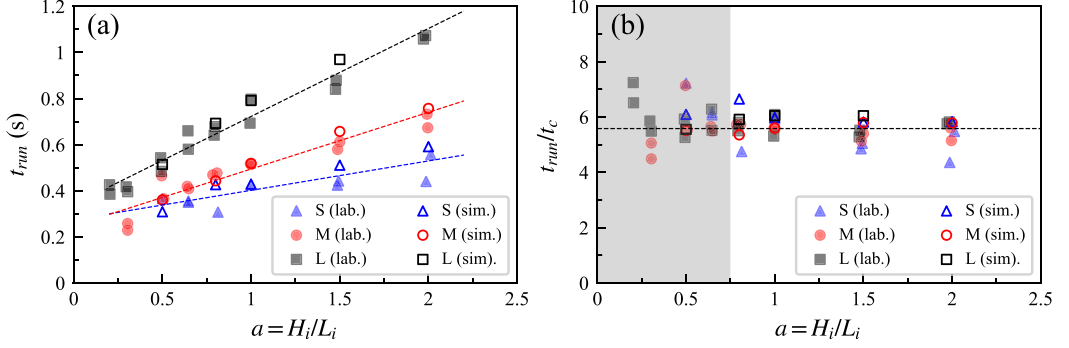


FIG. 7. (a) Variations of the runout duration  $t_{\text{run}} = t_{95} - t_{\text{trig}}$  with the aspect ratio  $a = H_i/L_i$ . The times  $t_{95}$  and  $t_{\text{trig}}$  are defined in Fig. 4. The dashed lines are the linear fit of the data for three different column sizes. The color of dashed lines matches the color of data points. (b) Plot of the runout duration normalized by the characteristic time  $t_c = \sqrt{H_i/g}$  against the aspect ratio. The horizontal dashed line indicates the averaged values for  $t_{\text{run}}/t_c$  (from both experiments and simulations with different column sizes) when  $a > 0.75$ .

collapse with each other very well. There are mainly two reasons. First, the assumption of free fall might not be very relevant for shallow granular collapses. Second, the measurement of  $t_{\text{trig}}$  is prone to error due to the gate removal effect (see Sec. II B), especially when the aspect ratio is small and there are fewer particles across the column height. Although the triggering process in general is quite short, the fluctuations in the measurement of  $t_{\text{trig}}$  may lead to variations in  $t_{\text{run}}$ . Moreover, the influence of  $t_{\text{trig}}$  could be amplified when  $t_{\text{run}}$  is relatively small in shallow granular collapses. When  $a > 0.75$ , the normalized runout duration  $t_{\text{run}}/t_c$  remains almost constant as the aspect ratio varies. The averaged values for  $t_{\text{run}}/t_c$  from both experiments and simulations with different column sizes are calculated to be 5.6, which is indicated by the horizontal dashed lines in Fig. 7(b). We can conclude, therefore, that the difference in the normalized runout distance caused by the change of column size is mainly due to the different spreading velocity after normalization. In this study, the normalized runout duration  $t_{\text{run}}/t_c$  falls into a range that is similar to the previous results for aspect ratios varying from 0.5 to 8 for both dry and underwater cases (simulated with the CFD-DEM methodology) presented in [11]. This indicates that the normalized runout duration lying between 4 and 8 is likely a robust feature of free-fall and fluid-inertia dominated granular column collapses, regardless of the initial aspect ratio, the sample size, and the ambient fluid (as long as the buoyancy effect is taken into account). However, the runout duration normalized by  $t_c$  could be an order of magnitude higher if fluid viscous effects are the prominent mechanisms, according to the experimental measurements conducted by Bougouin and Lacaze [6]. Note that the runout duration is also heavily dependent on the initial packing density in immersed granular collapses, with larger values in denser initial states [15, 17, 18].

### E. Mobility from numerical results

One advantage of the LBM-DEM model is that it keeps track of particle positions at every time step. To examine the effects of column size on the flow mobility of underwater granular collapses, the particles are painted according to their displacements in the  $xy$ -plane ( $\delta_{xy}$ ) after deposition and Figs. 8(a) and 8(b) plot the colored particles of small and large granular columns at their original positions for  $a = 1$ . The particle displacement increases gradually from the bottom-left corner to the top-right corner. Although the percentage of stationary particles ( $\delta_{xy} \leq d_p$ ) is comparable between the small and the large cases [see the black basal wedges in Figs. 8(a) and 8(b)], there are more particles in the larger case reaching a longer distance (e.g., see yellow particles).

Unlike the runout distance discussed in Sec. IV C, which is a local measurement that depends only on the front position, the movement of the center of mass of a granular assembly indicates the

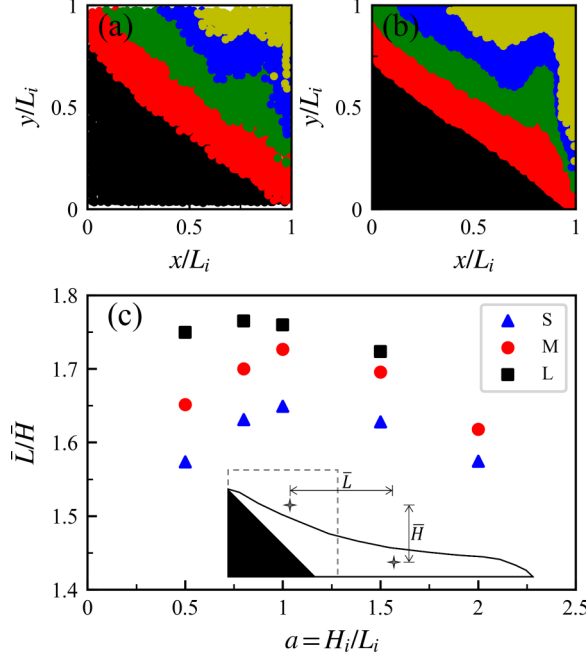


FIG. 8. Numerical results: (a), (b) Particles at their initial positions from the small ( $L_i = 3$  cm) and the large ( $L_i = 10$  cm) granular collapses when  $a = 1$ . The particles are painted according to their displacements in the  $xy$ -plane: black ( $\delta_{xy} \leq d_p$ ), red ( $d_p < \delta_{xy} \leq 0.5L_i$ ), green ( $0.5L_i < \delta_{xy} \leq L_i$ ), blue ( $L_i < \delta_{xy} \leq 1.5L_i$ ), yellow ( $\delta_{xy} > 1.6L_i$ ). (c) Comparison between underwater granular collapses with different column sizes in terms of the flow mobility  $\bar{L}/\bar{H}$  at various aspect ratios. The inset of (c) sketches the centers of mass of the flowing particles at their initial and final positions, and their difference in horizontal ( $\bar{L}$ ) and vertical ( $\bar{H}$ ) directions.

overall flow mobility. The tracking of particle positions in simulations allows us to calculate the center of mass of a granular assembly accurately at any instant of time and within any predefined spatial domain, which is not possible in the experiments. In this study, the underwater granular collapse is considered as a small landslide event in which the interface between the stationary (black) and moving (other colors) particles depicts a sliding plane, and the top mass slides down a basal wedge and transforms into a horizontal spreading until the final deposition. We characterize the overall flow mobility by the transport of the center of mass of the flowing particles. The inset of Fig. 8(c) sketches the outlines of the initial column (dashed line) and the final deposit (solid line). The centers of mass of the flowing particles at their initial and final positions are indicated by the star symbols. The changes of the center of mass in the horizontal and vertical directions are denoted as  $\bar{L}$  and  $\bar{H}$ , respectively. Then the ratio of  $\bar{L}$  over  $\bar{H}$  can be used to measure the overall granular flow mobility, which is plotted against the aspect ratio in Fig. 8(c). Interestingly, as the aspect ratio increases, the granular flow mobility ( $\bar{L}/\bar{H}$ ) first increases to a maximum at  $a \approx 1$ , and then decreases. It is likely due to the fact that when  $a$  is small and as it increases,  $\bar{H}$  increases slowly with the final deposit being trapezoidal. In this case, the increase of  $\bar{L}$  dominates and the ratio  $\bar{L}/\bar{H}$  increases. By contrast, the drop of the center of mass rises up rapidly when  $a > 1$  and only a small portion of particles at the front can travel to a long runout distance. As a result, the overall flow mobility  $\bar{L}/\bar{H}$  decreases. More importantly, for the same initial aspect ratio, the granular flow mobility has a positive correlation with the column size in underwater granular collapses.



## V. UNDERSTANDING THE SIZE EFFECTS

This section is intended to provide explanations to the size-dependent flow mobility in underwater granular collapses, as presented in Sec. IV, based on the rich numerical data from LBM-DEM simulations. The potential and kinetic energies are first extracted to quantify the column size effects on the collapse dynamics. Then the local flow properties, including the spatial distribution of fluid and particle velocities, the interparticle contact forces, and the basal slip velocities, are presented to uncover the column size effects at the particle scale.

### A. Energy evolution

The energy evolution of granular collapses has been utilized as an indicator for flow regime transitions caused by the aspect ratio and the initial packing density in our previous studies [11,18]. In granular collapses, the particles are subjected to different forces, namely, gravity, contact forces (including friction), buoyancy, and fluid drag. The avalanches of particles are initiated by the force unbalance caused by the gate removal. Gravity acts as the major driving force and does positive work, resulting in a drop of the particle potential energy. In LBM-DEM simulations, it is straightforward to calculate the total potential energy ( $E_h$ ) at a certain instant of time  $t$ , defined as

$$E_h(t) = \sum_{j=1}^{N_p} m_{p,j} g' h_j(t), \quad (11)$$

where  $m_{p,j}$  and  $h_j$  are the mass and height of the  $j$ th particle, respectively, and  $N_p$  is the total number of particles. Note that the reduced gravitational acceleration has been applied in Eq. (11) to account for the net effect of gravity and buoyancy. Thus, the cumulative potential energy loss can be calculated as

$$\Delta E_h(t) = E_h(0) - E_h(t). \quad (12)$$

Following Jing *et al.* [11], we assume that the elastic potential energy stored at the particle contacts (the overlap of particles is small in DEM simulations) and the rotational particle kinetic energy are negligible. Then, the change of total potential energy  $\Delta E_h$  is either transformed into the translational kinetic energy of particles ( $E_k^p$ ) and the fluid ( $E_k^f$ ) or dissipated by inelastic interparticle interactions (i.e., sliding and damping) and by the fluid viscosity. Therefore, the cumulative dissipated energy ( $E_d$ ) can be approximated as

$$E_d(t) = \Delta E_h(t) - [E_k^p(t) + E_k^f(t)]. \quad (13)$$

The kinetic energies can be calculated according to the masses and velocities of particles and fluid cells:

$$E_k^p = \frac{1}{2} \sum_{j=1}^{N_p} m_{p,j} (|\mathbf{u}_p|_j)^2, \quad (14)$$

$$E_k^f = \frac{1}{2} \sum_{j=1}^{N_f} (1 - \varepsilon_j) m_{f,j} (|\mathbf{u}_f|_j)^2, \quad (15)$$

where  $\mathbf{u}_p$  and  $\mathbf{u}_f$  are the macroscopic particle and fluid velocities, respectively. Note that  $\mathbf{u}_p$  (velocity at the particle center) is different from the solid velocity  $\mathbf{u}_s$  in Eq. (7), which is also a function of the angular particle velocity and the location of the fluid cell. The total number of fluid cells is denoted by  $N_f$ . The mass of a fluid cell is denoted by  $m_f$ , which may change slightly across different fluid cells due to the small compressibility of the LBM formulation [35]. To account for the solid and partially saturated fluid cells, a prefactor  $1 - \varepsilon$  has been applied in Eq. (15), where  $\varepsilon$  is the solid coverage ratio (see Sec. III).

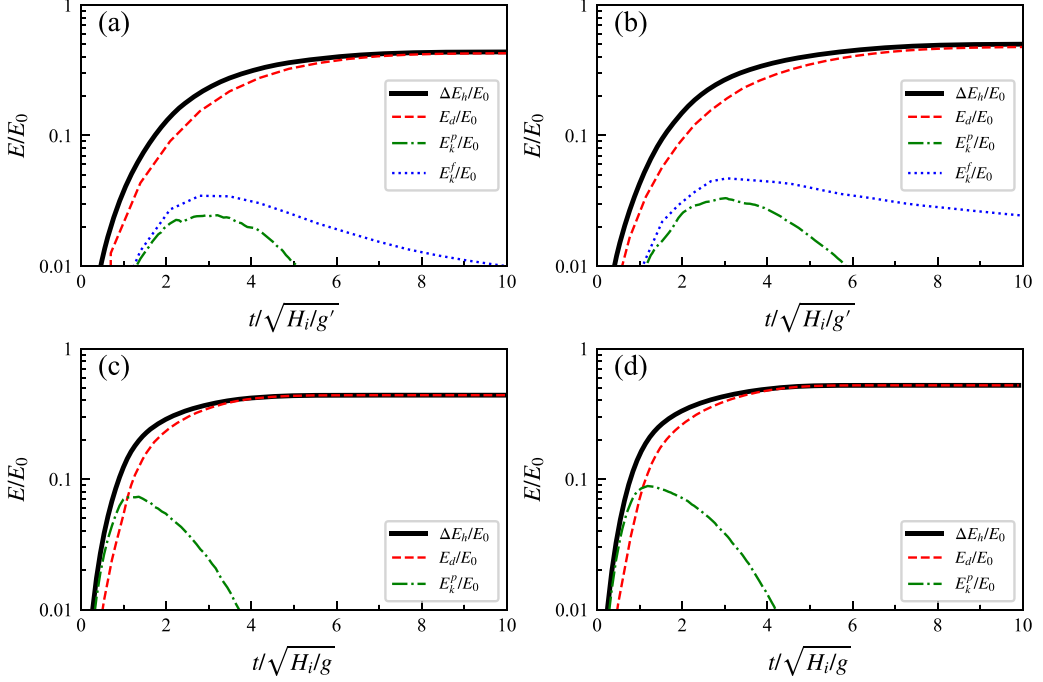


FIG. 9. Numerical results: temporal evolution of the cumulative potential energy loss  $\Delta E_h$ , the cumulative dissipated energy  $E_d$ , the particle kinetic energy  $E_k^p$ , and the fluid kinetic energy  $E_k^f$  (if applicable) normalized by the initial total potential energy  $E_0$  in (a) small ( $L_i = 3$  cm, underwater), (b) large ( $L_i = 10$  cm, underwater), (c) small ( $L_i = 3$  cm, dry), and (d) large ( $L_i = 10$  cm, dry) granular column collapses for  $a = 1$ .

Figure 9 compares collapses of small and large granular columns in dry and underwater conditions regarding the temporal evolution of the energies as a fraction of the initial potential energy [ $E_0 = E_h(0)$ ] for  $a = 1$ . When the column size is small ( $L_i = 3$  cm), about 43% of the initial potential energy is transformed or dissipated throughout the granular collapse process in the underwater condition as shown in Fig. 9(a). The particle kinetic energy  $E_k^p$  first increases during the acceleration stage (defined in Fig. 4), reaching a peak of  $2.4\%E_0$  (short for 2.4% of  $E_0$ ) at  $t \approx 3t_c$ . Then the particles gradually slow down until their kinetic energy vanishes and the final deposit is formed. The movement of the particles can set the surrounding fluid into motion and thereby transfers kinetic energy to the fluid phase continuously. Furthermore, a large percentage of the particle kinetic energy is dissipated via inelastic interparticle collision and sliding, thus the fluid kinetic energy accumulates and reaches a higher peak ( $3.5\%E_0$ ) compared to the maximum  $E_k^p$  but roughly at the same moment ( $t \approx 3t_c$ ). Also, Fig. 9(a) shows that the rate of dissipation of the fluid kinetic energy  $E_k^f$  is much lower than that of the particle kinetic energy  $E_k^p$ . As a result,  $E_k^f$  persists much longer, and maintains its value of  $1.0\%E_0$  at around  $10t_c$  even after the final deposition of particles. This fluid kinetic energy is carried mainly by the induced eddies, which will be discussed in Sec. V D.

When the granular column increases from the small to the large size in the underwater condition, the cumulative potential energy loss after the final deposition rises up to  $50\%E_0$  [see Fig. 9(b)]. It means that there is more energy available for the propagation of particles. Thus, the peak fluid and particle kinetic energies also increase to  $4.7\%E_0$  and  $3.3\%E_0$ , respectively. However, the time when the peak kinetic energies occur is almost unchanged, i.e.,  $t \approx 3t_c$ . Besides, it takes an even longer time for the dissipation of the fluid kinetic energy in the large case, with  $E_k^f$  more than  $2.4\%E_0$  at  $t = 10t_c$ .

In the dry condition, there is a significant increase of the cumulative potential energy loss as the column size increases, as shown in Figs. 9(c) and 9(d). More quantitatively, the cumulative potential energy loss after the final deposition rises up from  $44\%E_0$  to  $52\%E_0$  as  $L_i$  increases from 3 to 10 cm. The amount of increase (8%) is similar to that in the underwater condition. Meanwhile, the peak particle kinetic energy  $E_k^p$  increases by 37.5% and 20.5% in underwater and dry granular collapses, respectively, as the column size increases. That means, the peak particle kinetic energy increases with the column size to a lesser extent in the dry condition when compared to the underwater cases.

### B. Partial kinetic energy

To have a better understanding of the collapse dynamics from vertical fall to horizontal spreading, we calculate the kinetic energy based on velocities in the  $x$  and  $y$  directions. For the particles, we have

$$E_{kx}^p = \frac{1}{2} \sum_{j=1}^{N_p} m_{p,j} u_{p,j}^2, \quad (16)$$

$$E_{ky}^p = \frac{1}{2} \sum_{j=1}^{N_p} m_{p,j} v_{p,j}^2. \quad (17)$$

The vertical and horizontal partial kinetic energies for particles are denoted as  $E_{kx}^p$  and  $E_{ky}^p$ , respectively. The velocity components of the  $j$ -th particle in the  $x$  and  $y$  directions are  $u_{p,j}$  and  $v_{p,j}$  correspondingly. For the fluid, the horizontal and vertical kinetic energies ( $E_{kx}^f$  and  $E_{ky}^f$ ) can be calculated as

$$E_{kx}^f = \frac{1}{2} \sum_{j=1}^{N_f} (1 - \varepsilon_j) m_{f,j} u_{f,j}^2, \quad (18)$$

$$E_{ky}^f = \frac{1}{2} \sum_{j=1}^{N_f} (1 - \varepsilon_j) m_{f,j} v_{f,j}^2, \quad (19)$$

where  $u_f$  and  $v_f$  are the fluid velocity components in the  $x$  and  $y$  directions, respectively.

Figures 10(a) and 10(b) compare the small and the large underwater granular collapses with  $a = 1$  in terms of the temporal evolution of the partial kinetic energies. When the small column collapse is considered, as shown in Fig. 10(a), the vertical particle kinetic energy  $E_{ky}^p$  increases at a faster rate than the horizontal particle kinetic energy  $E_{kx}^p$ , indicating a predominant falling behavior under gravity at the early stage. The vertical particle kinetic energy  $E_{ky}^p$  reaches a peak of  $1.1\%E_0$  at around  $t = 2t_c$ . After that, the particle motion is gradually redirected to the horizontal direction and part of  $E_{ky}^p$  is transferred to  $E_{kx}^p$ . As a result, the horizontal particle kinetic energy  $E_{kx}^p$  continues to rise up to a higher peak of  $1.8\%E_0$  at around  $t = 3.5t_c$ . The efficiency of conversion from  $E_{ky}^p$  to  $E_{kx}^p$  is closely related to the flow mobility during the propagation stage, which will be discussed in detail in Sec. V C. The temporal evolution of the partial kinetic energies of the fluid is rather similar to that of particles, except that the peaks of  $E_{kx}^f$  and  $E_{ky}^f$  are higher and the occurrence of maximum  $E_{ky}^f$  is slightly delayed.

When the column size becomes larger ( $L_i = 10$  cm), all the peak partial kinetic energies normalized by the initial potential energy increase by at least 26%. However, the moments when the peak partial kinetic energies take place are roughly the same, as shown in Fig. 10(b). In the large granular column collapse, there seems to be a period of constant horizontal particle kinetic energy (between  $3t_c$  and  $4t_c$ ). During this period, the horizontal kinetic energy gained from the conversion of vertical kinetic energy and the drop of potential energy is well balanced by the energy dissipated via inelastic particle interactions and the fluid drag. Our numerical results show that this balanced

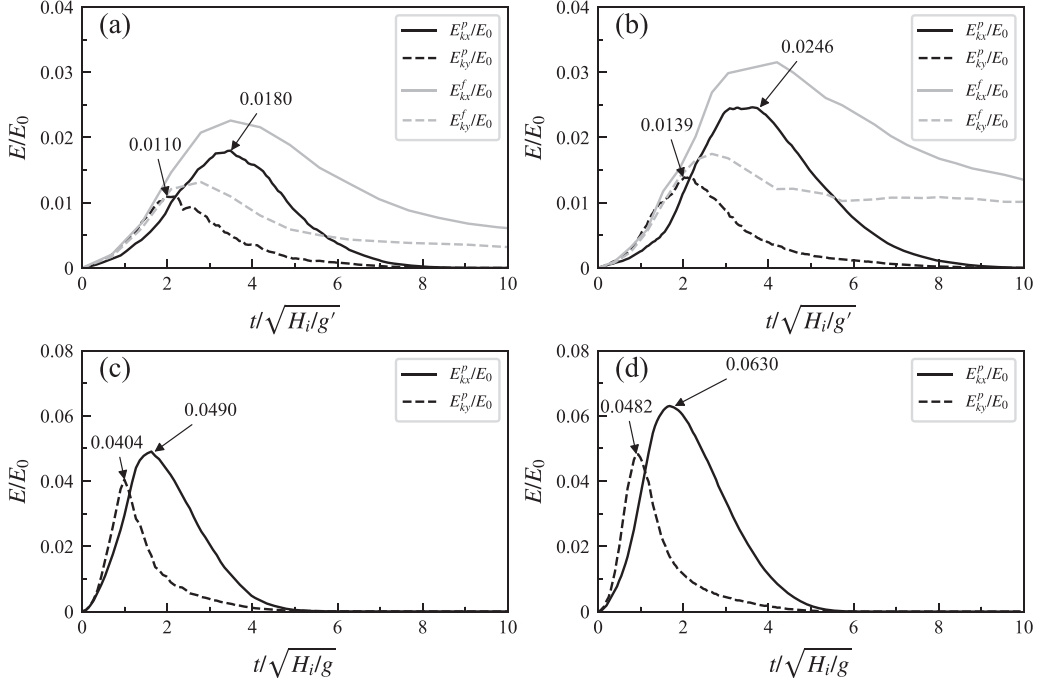


FIG. 10. Numerical results: temporal evolution of the partial kinetic energies computed from the  $x$  and  $y$  components of the fluid (if applicable) and particle velocities in (a) small ( $L_i = 3$  cm, underwater), (b) large ( $L_i = 10$  cm, underwater), (c) small ( $L_i = 3$  cm, dry), and (d) large ( $L_i = 10$  cm, dry) granular column collapses for  $a = 1$ .

state is too short-lived to reveal itself in the small underwater granular collapse [see Fig. 10(a)]. In the dry cases, the increase of column size from small to large results in 19.3% and 28.6% increase for the peak vertical and horizontal particle kinetic energies, respectively, as shown in Figs. 10(c) and 10(d). Similar to the total particle kinetic energy discussed in Sec. V A, the size effect on the partial particle kinetic energies is less significant in the dry condition compared to those in the underwater condition.

### C. Energy conversion

It was argued by Topin *et al.* [13] that the peak horizontal kinetic energy of particles ( $\max E_{kx}^p$ ) determines the overall granular flow mobility. The value of  $\max E_{kx}^p$  is heavily dependent on the ability of granular collapses to transfer the kinetic energy from vertical to horizontal directions [11]. The peak partial kinetic energies of particles ( $\max E_{kx}^p$  and  $\max E_{ky}^p$ ) are extracted in all underwater simulations and plotted against the aspect ratio  $a$  in Fig. 11(a). For the range of aspect ratios tested in this study, the peak vertical kinetic energy  $\max E_{ky}^p$  is notably smaller than the peak horizontal kinetic energy  $\max E_{kx}^p$ , probably due to the weaker vertical inertial characteristic of the relatively shallow initial condition. Both  $\max E_{kx}^p$  and  $\max E_{ky}^p$  normalized by the total initial potential energy  $E_0$  increase as the aspect ratio increases. In addition, the normalized  $\max E_{kx}^p$  and  $\max E_{ky}^p$  also become larger when the column size increases.

To better examine the efficiency of energy conversion from vertical to horizontal directions, the ratio of  $\max E_{kx}^p$  over  $\max E_{ky}^p$  is plotted against the aspect ratio  $a$  in Fig. 11(b). The ratio  $\max E_{kx}^p / \max E_{ky}^p$  first increases with the aspect ratio, reaching a maximum at around  $a = 1.5$ , which agrees with previous CFD-DEM results [11]. Then, the ratio  $\max E_{kx}^p / \max E_{ky}^p$  slightly decreases as

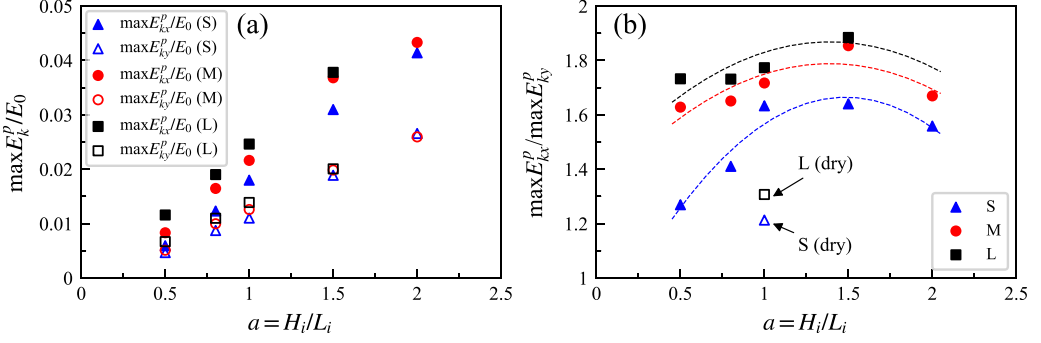


FIG. 11. Numerical results: plots of (a) the peak partial kinetic energies of particles ( $\max E_{kx}^p$  and  $\max E_{ky}^p$ ) normalized by the initial total potential energy  $E_0$  and (b) the ratio between  $\max E_{kx}^p$  and  $\max E_{ky}^p$  against the aspect ratio  $a$  for granular collapses with different column sizes. Trend (dashed) lines are drawn to help the comparison. The hollow symbols are the results from dry granular column collapses.

$a$  increases from 1.5 to 2. Actually, it is expected that the ratio  $\max E_{kx}^p/\max E_{ky}^p$  will continue to drop (to even below 1) as  $a$  further increases, due to the stronger vertical inertial effect at higher aspect ratios and a huge amount of kinetic energy is lost when the falling particles collide with the bottom stagnant materials [11]. More importantly, Fig. 11(b) shows that underwater granular collapses of larger columns are able to convert the particle kinetic energy from vertical to horizontal directions more efficiently, resulting in a larger  $\max E_{kx}^p$  that contributes to the horizontal spreading, which explains the enhanced granular flow mobility observed in our experiments and simulations (see Sec. IV).

Although water drains energy from the granular phase via fluid drag, resulting in smaller particle kinetic energies in the underwater cases (see Fig. 9), it is interesting to note that the ratio  $\max E_{kx}^p/\max E_{ky}^p$  is generally smaller in the dry condition [see the hollow symbols in Fig. 11(b)]. That means the interstitial fluid in the underwater condition helps the transfer of particle kinetic energy from vertical to horizontal directions in a more efficient manner. Furthermore, similar to the size effect on each component of the particle kinetic energies, there is a more significant increase of energy conversion efficiency in the underwater condition as the granular column enlarges from a small to a large size, highlighting the important role of the interstitial water.

To provide micromechanical explanations to the above-mentioned energy arguments about the column size effects on the granular flow mobility, we explore local flow properties of both the solid and fluid phases.

#### D. Solid volume fraction and velocity fields

The high spatial and temporal resolutions of the LBM-DEM model allow us to get access to the local characteristics of the fluid and particle fields. Figure 12 compares the small and large underwater granular collapses regarding the distributions of solid volume fraction, particle and fluid velocities for the aspect ratio  $a = 1$ . The results at a typical instant of time  $t = 3t_c$  are picked for comparison, at which the flow is rather active with high kinetic energy (see Figs. 9 and 10). The spatial distributions of solid volume fraction are plotted in Figs. 12(a) and 12(b). Although the surfaces of the granular particles are quite smooth, there is a sudden change of slope at around  $x/L_i = 1.3$  just behind the granular front (called a “granular heave” herein).

Such granular heaves are also observed in our experiments (see Fig. 2 and the supplemental videos [47]), which stem from the secondary transport of particles close to the granular free surface [see Figs. 12(c) and 12(d) for the vector fields of particle velocities]. At the location of the granular heave, there is a strong circulation motion of particles observed only in the large granular collapse, indicating an unscaled and stronger fluid inertial effect as the column size increases. It is also

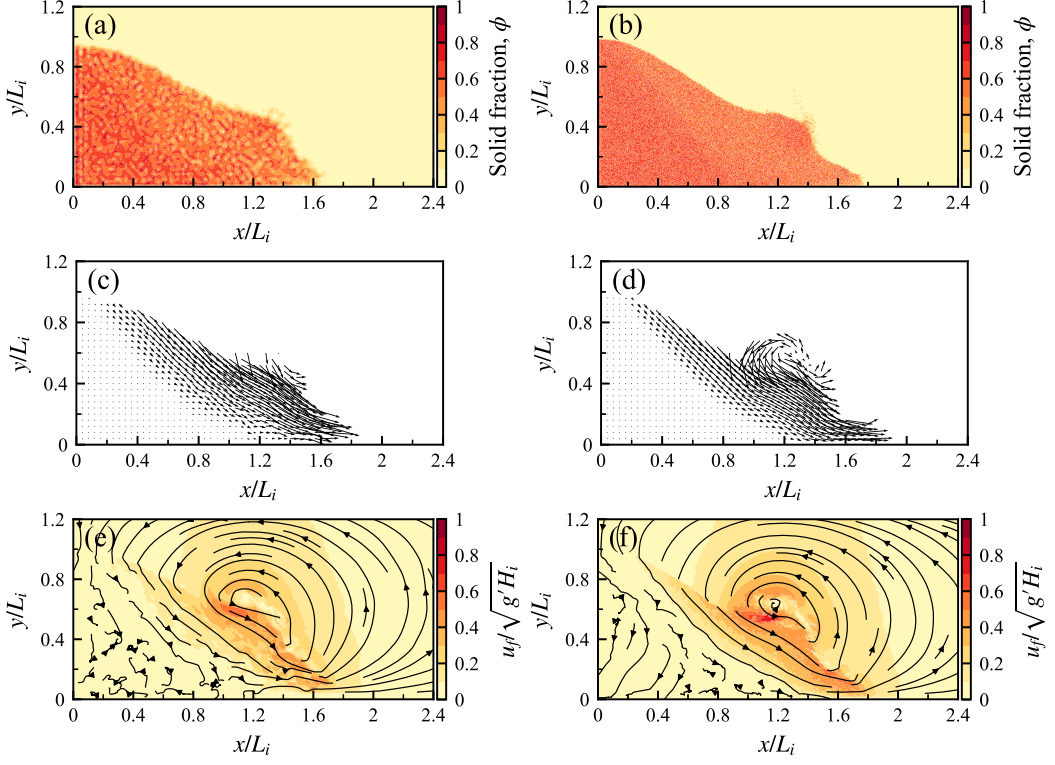


FIG. 12. Numerical results: comparison between the small (left panel) and large (right panel) underwater granular collapses ( $a = 1$ ) regarding (a), (b) the spatial distribution of solid volume fraction; (c), (d) the vector field of the particle velocity; and (e), (f) the fluid streamlines and the spatial distribution of the fluid velocity magnitude, when  $t = 3t_c$ .

evidenced by the larger fluid velocity (normalized by  $\sqrt{g'H_i}$ ), as shown in Figs. 12(e) and 12(f). More quantitatively, the maximum fluid velocity induced by granular collapse increases from 0.284 to 0.764 m/s as the column size increases from 3 to 10 cm. It means that the fluid velocity scales by a factor of 2.7 when the characteristic velocity ( $\sqrt{g'H_i}$ ) is increased by only 1.8 times. In other words, when the size of the granular column increases, the velocity increases disproportionately with respect to the characteristic velocity scale by a factor of 1.5.

### E. Fluid drag

The unscaled fluid inertia can affect the fluid drag acting on the flowing particles. Figures 12(e) and 12(f) show that the fluid eddy penetrates through the upper portion of the granular flow and has a tendency to accelerate the particles (the fluid and particles follow the same flow direction moving forward). Borrowing the idea of drag models, in which the fluid drag force is usually calculated as the relative fluid-particle velocity multiplied by a drag coefficient, we can use the relative velocity,  $\mathbf{u}_f - \mathbf{u}_p$ , as an indicator for the magnitude and direction of the fluid drag force. Note that while we consider the hydrodynamic drag as the major fluid-particle interaction force that dissipates the particle kinetic energy [48], other fluid effects such as added mass, lift, or Basset history forces may also be relevant in such transient flows [49].

Figure 13 compares the small and the large granular collapses in terms of the relative fluid-particle velocity in the  $x$ -direction. Before taking the difference, both  $u_f$  and  $u_p$  have been averaged according to the  $x$  and  $y$  coordinates of the fluid cells and particles within query windows of size



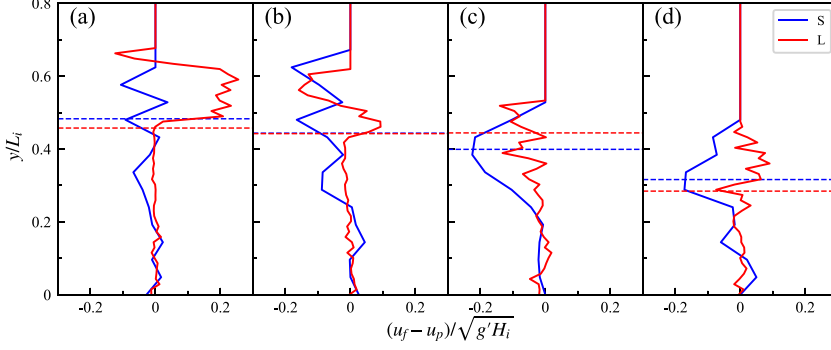


FIG. 13. Numerical results: relative fluid-particle velocity ( $x$  component) profiles of small and large granular collapses ( $a = 1$ ) at the cross sections: (a)  $x/L_i = 1.3$ , (b)  $x/L_i = 1.35$ , (c)  $x/L_i = 1.4$ , (d)  $x/L_i = 1.45$ . The fluid and particle velocities are averaged over  $0.2t_c$ . The horizontal blue and red dashed lines separate the dense granular flow region and the dilute suspended particle region for the small and large granular collapses, respectively. The region with zero relative velocity is the pure water region.

$d_p$ . That means the velocities are also averaged along the  $z$ -direction. It has been checked that averaging in query windows of different sizes, as long as they are small enough and the averaging still represents the local flow property, will produce similar results. As well, both  $u_f$  and  $u_p$  are averaged over a time period of  $0.2t_c$ , i.e., from  $2.9t_c$  to  $3.1t_c$ . We focus on four different cross sections close to the front where  $x/L_i = 1.3, 1.35, 1.4$  and  $1.45$ . The relative velocity profiles at slightly different cross sections are similar and will not alter the conclusions in the following.

During the propagation stage at around  $t = 3t_c$ , the gravity-induced acceleration of particles becomes weak (see Fig. 9). The motion of particles is mainly maintained by the horizontal momentum and the particle kinetic energy is gradually dissipated via various mechanisms, including the fluid drag. When the column size is small, the relative velocity  $u_f - u_p$  is in general negative (see the solid blue lines in Fig. 13), especially within the flowing region, indicating that the motion of fluid flow is *passively* driven by the moving particles. In other words, the fluid viscous drag poses an additional resistance to the propagation of particles and has a negative impact on the granular flow mobility. In the large granular collapse, the relative velocity  $u_f - u_p$  not only increases significantly (see the solid red lines in Fig. 13), but also becomes positive in some areas close to the granular surface and the dilute suspended particle region. This is a signature of the larger horizontal fluid kinetic energy in larger collapses and its consequence is that the particles are now carried by the moving fluid eddy originally generated by their motion, as shown in Fig. 12(f). That means the fluid eddy grows to be strong enough to *actively* drive the particles close to the granular surface forward, thereby enhancing the overall granular flow mobility.

#### F. Lubrication and basal slip

Apart from the unscaled fluid inertia and the fluid drag, the distinct collapse dynamics of small and large granular columns could be caused by contact lubrication [13]. For dry dense granular collapses, the energy dissipation should scale monotonically with the column size according to the Mohr-Coulomb model if one assumes interparticle friction to be the major resistance and a constant friction coefficient [50]. However, it is well known that the apparent friction coefficient is highly dependent on the local shear rate and stress state [48,51], which will affect the energy dissipation as the column size changes. In addition, the interstitial fluid in underwater cases may have an extra lubrication effect that reduces the contact friction and thereby altering the flow mobility, which can be innately captured by our LBM-DEM model [33].

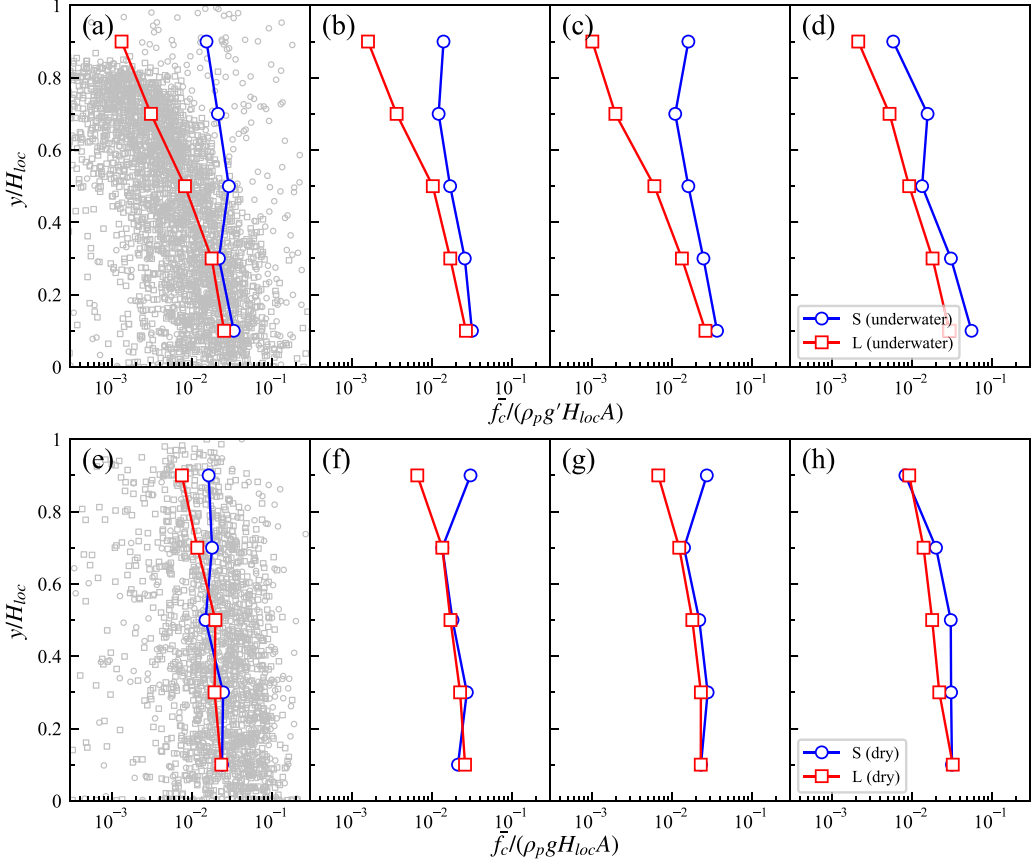


FIG. 14. Numerical results: spatial distribution of the locally averaged and time-averaged interparticle contact force  $\bar{f}_c$  normalized by a characteristic force based on the hydrostatic solid pressure at four sections:  $L_i = 1.3, 1.35, 1.4$  and  $1.45$  in (a)–(d) underwater and (e)–(h) dry granular collapses with small and large sizes.

Figure 14 compares underwater and dry granular collapses with different column sizes at  $a = 1$  in terms of the contact force profiles. Similar to the relative velocity profiles shown in Fig. 13, the contact force profiles at four sections close to the front,  $x/L_i = 1.3, 1.35, 1.4$ , and  $1.45$ , are extracted and the contact forces are also averaged over a time period from  $2.9t_c$  to  $3.1t_c$ . The locally averaged and time-averaged contact force is denoted as  $\bar{f}_c$ . In this study, we specifically choose a force scale characterized by the hydrostatic solid pressure,  $\rho_p g' H_{loc} A$  for the underwater cases and  $\rho_p g H_{loc} A$  for the dry cases, where  $H_{loc}$  is the local flow depth at a specific section and  $A = 2d_p l_z$  is the area of the measurement region. This normalization cancels out the intrinsic size effect on the interparticle contact force. In Figs. 14(a) and 14(e), the raw data are also presented with the same symbols as the averaged values in gray. A close examination of the raw data shows that the interparticle contact force follows a log-normal distribution. Interestingly, it is found that the averaged and normalized contact force decreases when the column size increases in both underwater and dry conditions, indicating a size-induced contact lubrication. Furthermore, such lubrication effects appear to be more prominent in the underwater condition. It has been checked that this is a robust trend that exists at other locations, and at other time instants as long as the flow is still active (the contact force profiles collapse for different column sizes when the flow stops).

One direct consequence of the contact lubrication is that particles tend to slip more at the base. Figures 15(a) and 15(b) compare the small and the large granular collapses in terms of

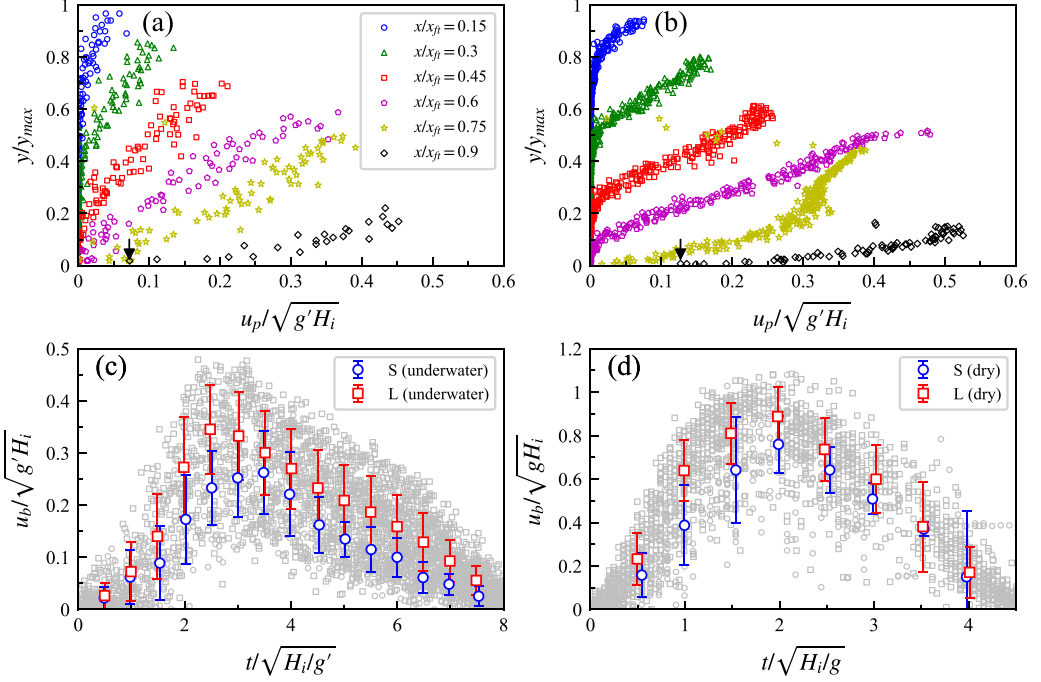


FIG. 15. Numerical results: comparison between (a) the small and (b) the large underwater granular collapses for the normalized particle velocity profiles at cross sections  $x/x_{ft} = 0.15, 0.3, 0.45, 0.6, 0.75, 0.9$ , when  $a = 1$  and  $t = 3t_c$ . The particle positions are normalized by the maximum flow thickness,  $y_{\max}$ . Plots in (c) and (d) compare the temporal evolution of the normalized basal slip velocity for underwater and dry granular collapses with different column sizes, respectively.

the normalized particle velocity profiles at  $t = 3t_c$ . First of all, the particle velocity profiles of underwater granular collapses are quite similar to those measured in dry granular collapses [7]. Close to the granular front, the flow is active throughout the whole flow thickness with a finite basal slip velocity, which can also be seen in Figs. 12(c) and 12(d). Farther away from the front, the particle velocity profiles consist of a linear portion with a constant shear rate within the flowing layer beneath the granular free surface and an exponential decay inside the lower static zone. Note that the high-intensity fluid eddy in the large granular collapse can alter the particle velocity profiles significantly, especially close to the granular heave [see Fig. 15(b) where  $x/x_{ft} = 0.6$  and  $0.75$ ]. It is interesting to find that the normalized basal slip velocity close to the front [highlighted by the arrows in Figs. 15(a) and 15(b)] is notably larger in the large granular collapse.

In order to further confirm the enhanced basal slip in the larger case, we have examined the velocity of particles within a thin layer ( $y < 0.05H_i$ ) above the base and close to the front ( $x > 0.9x_{ft}$ ), which is defined as the basal slip velocity  $u_b$ . Note that the thin layer we define is very close to the bottom (within one to three particle diameters). Also, although we focus on the front region, results are similar in other regions behind the front as long as particles there are sliding over the bottom. The temporal evolution of  $u_b$  normalized by the velocity scale  $\sqrt{g'H_i}$  is plotted in Fig. 15(c) for the small and the large underwater granular collapses. The raw data are shown at the background in gray, with the symbols matching those of the error bars. The error bars present the mean values of the normalized basal slip velocity at the selected sections, together with their standard deviations. It is found that the normalized basal slip velocity is noticeably larger when the column size increases. More quantitatively, the maximum averaged basal slip velocity is  $0.26\sqrt{g'H_i}$  and  $0.35\sqrt{g'H_i}$  for the small and the large cases, respectively. Figure 15(d) shows the

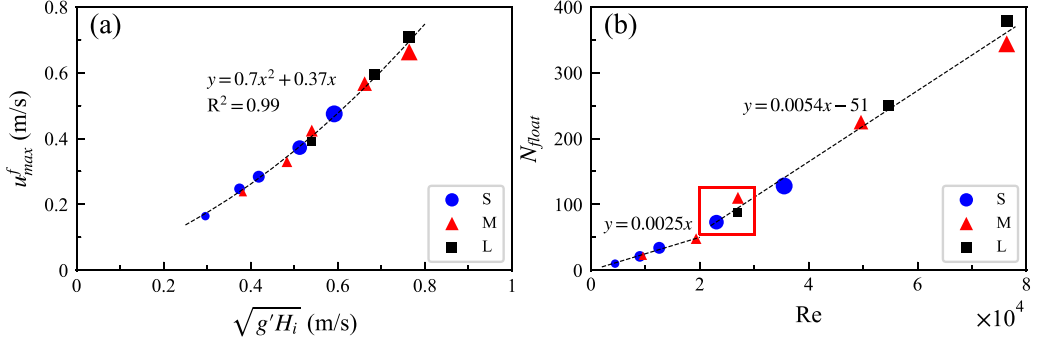


FIG. 16. Numerical results: (a) correlation between the maximum fluid velocity  $u_{max}^f$  that occurs in the eddies and the characteristic velocity  $\sqrt{g'H_i}$ ; (b) plot of the maximum number of suspended particles against the Reynolds number  $Re = g^{1/2}H_i^{3/2}/\nu_f$  based on the initial column height. The symbol size is proportional to the magnitude of initial aspect ratio.

temporal evolution of the normalized basal slip velocity,  $u_b/\sqrt{g'H_i}$ , from small and large dry granular collapses. Compared to the size effect on basal slip in the underwater condition, the influence in the dry condition is much smaller. More specifically, the basal slip velocity increases by 12% and 44% on average as the column size increases from  $L_i = 3$  to 10 cm in dry and underwater granular collapses, respectively. The difference could be caused by the extra lubrication provided by the interstitial fluid in the underwater cases, as shown in Fig. 14.

### G. Size-induced flow regime transition

The formation of strong eddies and granular heaves in large granular collapses are clear evidence of the more significant fluid inertial effect, which is partly responsible for the unscaled fluid velocity and drag force as the column size increases. This is an indication of flow regime transition solely caused by the change of column size with all the other parameters kept constant. In the phase diagram proposed by Courrech du Pont *et al.* [5], flow regimes are determined based on two dimensionless numbers, the Stokes number  $St$  and the particle-to-fluid density ratio  $r$ . The ratio between  $St$  and  $r$  can be defined as the Reynolds number, characterizing the relevant importance of fluid inertial and viscous effects. These dimensionless numbers are defined according to the ratio of timescales obtained from the dynamics of a *single grain* subjected to a driving force (normally gravity) and a drag force (depending on the flow regime). That means, the flow regime allows us to identify the dominant effect (i.e., grain inertia or free-fall, fluid inertia and fluid viscosity) at the *grain scale* only. In other words, the effects of flow regime on the collapse of a granular column at the macroscopic scale are not taken into account. Therefore, additional influence of column size on the flow regime, which has been observed in both our experiments and simulations, has to be considered.

Recently Bougouin and Lacaze [6] carried out experiments on the collapse of densely packed granular columns in different fluids. A *modified* phase diagram was defined in the  $((d_p/H_i)^{1/2}St, (d_p/H_i)^{1/2}r)$  space, making the flow regime depending on the initial column height  $H_i$ . However, there is still no clear description about the change of Reynolds number as  $H_i$  varies and about the way how the column-to-particle size ratio affects the flow regime. In order to examine the fluid inertia as the column size varies, an alternative Reynolds number based on the initial column height is defined. We choose  $H_i$  and  $\sqrt{g'H_i}$  as the characteristic length and velocity, respectively, because, as shown in Fig. 16(a), a unique and monotonic relationship between the maximum fluid velocity  $u_{max}^f$  and the characteristic velocity can be found, indicating that  $\sqrt{g'H_i}$  is an appropriate estimation of fluid inertial effect during underwater granular collapses. Therefore, the Reynolds number can

be written as  $Re = g'^{1/2} H_i^{3/2} / \nu_f$ , which will increase with the initial column height, resulting in a potential flow regime transition from viscous drag to fluid inertia as the dominant mechanism, matching our previous discussions about the size effects on runout scaling (see Sec. IV C).

A direct consequence of increased fluid inertia is the formation of strong eddies, which can carry the particles close to the granular free surface into suspension. To characterize this fluid inertia effect, the maximum number of suspended particles (denoted as  $N_{\text{float}}$ ) throughout the whole collapse process is extracted and plotted against the Reynolds number in Fig. 16(b). Note that a particle is regarded as suspended if its position is above the granular free surface. In general, there are more suspended particles as the Reynolds number increases with a sudden change of increasing rate at around  $Re = 20\,000$ . In other words,  $N_{\text{float}}$  increases more rapidly when  $Re$  is larger than 20 000 (the increasing rate is more than doubled), showing more significant fluid inertial effects. Note that there are roughly the same number of suspended particles at the same Reynolds number, regardless of the different initial aspect ratios and the different total volumes of the granular columns [see the cases enclosed by a red box in Fig. 16(b)], at least for the range of parameter variations explored in this study. These results demonstrate that the proposed  $Re$  is potentially an important dimensionless number governing the size-induced flow regime transition.

All in all, the unscaled fluid inertia, the fluid drag force, the contact lubrication and the basal slip are crucial evidences for the complex interplay between the interstitial fluid and the size of the granular flow, which can be used to account for the size-dependent granular flow mobility in underwater granular collapses. However, a more thorough parametric analysis, considering the complex interplay between the column size, particle size, packing density, fluid viscosity, and other factors, is needed to identify the relevant dimensionless numbers and the necessary conditions for the transition between different flow regimes, which will be studied in future work.

## VI. CONCLUSIONS

In this paper, we report an experimental and numerical study of the role of column size in underwater granular collapses. Experiments of underwater granular collapses with three different column sizes ( $L_i = 3, 5, 10$  cm) and the aspect ratio up to 2 have been carried out. To explain the size-dependent granular collapse dynamics at the grain scale, we simulate the underwater granular collapse experiments using a coupled lattice Boltzmann and discrete element method.

Snapshots of underwater granular collapses in experiments are extracted, showing fluid eddies carrying particles into suspension at large column sizes and aspect ratios, which is responsible for the wavy granular free surface of the final deposit. Within the range of aspect ratios considered in this study, it is found that the normalized runout distance  $\tilde{L}_f$  of underwater granular collapses scales linearly with the initial aspect ratio  $a$ ,  $\tilde{L}_f = \lambda a$ , which agrees with the previous experimental measurements [6]. As the column size increases, the coefficient of proportionality also increases by following the relation  $\lambda = 0.006 L_i / d_p + 1.63$ . In addition, a flow mobility index ( $\bar{L} / \bar{H}$ ) is defined according to the transport of the center of mass of the flowing particles during underwater granular collapses. There is a significant increase of granular flow mobility as the column size becomes larger. On average, the runout distance normalized by the initial column length ( $L_i$ ) and the flow mobility index increase by 18% and 22%, respectively, as  $L_i$  increases from 3 to 10 cm.

According to the numerical data with high spatial and temporal resolutions, we are able to clarify the size-dependent granular flow mobility from the energy perspectives. First, the cumulative potential energy loss increases from 43% to 50% of the initial potential energy as the granular column enlarges from the small to the large size. Based on the fact that gravity is the major driving force for the collapse of particles, a higher percentage of the potential energy is transferred to the particle kinetic energy in the large case. Furthermore, when the flow is redirected from the vertical to horizontal directions, the vertical particle kinetic energy can be transferred to the horizontal component in a more efficient manner when the column size is larger. As a result, the particles in larger underwater granular collapses gain more power (higher kinetic energy) for the horizontal spreading.

The local flow characteristics have been invoked to reveal the column size effects on the energy conversion that determines the granular flow mobility. When the column size increases, the fluid inertia becomes large enough to erode the granular surface, producing a granular heave just behind the front. Moreover, the strong fluid eddy in the large case penetrates through the flowing layer of the granular phase, which can push the particles forward via the fluid drag force. In addition, the interstitial water has an effect of lubricating the interparticle contacts, causing basal slip of the fast-moving granular front. By comparison, the basal slip velocity increases by 12% and 44% on average in dry and underwater granular collapses, respectively, as the granular column enlarges from the small to the large size. This contact lubrication or resistance reduction becomes more prominent as the column size increases, contributing to an enhanced granular flow mobility and a longer final runout distance.

The current study focuses on a limited range of column size in both experiments and simulations, due to the lack of laboratory space and computational power. It is essential to establish emerging constitutive laws in a continuum framework to extend our findings to a broader range of problem scales. Ideally, the constitutive model shall be able to capture all the complex interparticle and fluid-particle interactions at the grain scale, which automatically converges to the correct macroscopic flow behavior at any system size. The results presented in this study can be useful to validate such size-dependent continuum models and their establishment will be our next focus for bridging the micromechanics and the macroscopic flow behaviors.

#### ACKNOWLEDGMENTS

This research was conducted in part using the research computing facilities and/or advisory services offered by Information Technology Services, the Hong Kong University Grants Committee - General Research Fund (GRF), 17205821, and under the support of FAP-DF, Brazil. The NSFC Project (No. 42107154) and the Guangdong Science and Technology Project (No. 2020A1515110810) also support this work. We would like to thank N.C. Poon, H. Wu, and M. Tse for their help on the experiments.

#### APPENDIX: EFFECTS OF RANDOM SEED IN LBM-DEM SIMULATIONS

In order to make sure that the influence of random seed on the LBM-DEM results examined in this study is relatively small compared to the size effects, five repeated simulations with  $L_i = 5$  cm and  $a = 1$ , but with different random seeds are carried out. Figure 17(a) presents the final deposit profiles from the five repeated LBM-DEM simulations, together with the final deposit profiles from the small and large cases ( $L_i = 3$  and 10 cm at  $a = 1$ ) overlaying on top of each other. Generally speaking, the difference between the five repeated cases regarding the final deposit profile is rather small. A larger difference is observed at the frontal region where the fluid-particle interaction is stronger during the collapse. The minimum and maximum values for the normalized runout distance  $L_f/L_i$  are extracted and indicated by two black lines in Fig. 17(a). More specifically, the final normalized runout distance averaged among the five repeated simulations is 2.805 with the maximum and minimum values found to be 2.836 and 2.779, respectively. As a result, the range of variation is about 2% as a fraction of the mean value. By comparison, the normalized runout distance of the small and large column collapses is 2.65 and 3.05, respectively.

In addition, the temporal evolutions of the particle kinetic energy normalized by the initial potential energy from the five repeated LBM-DEM simulations, and the small and the large cases are plotted in Fig. 17(b). Again, the overall behavior is rather similar. The minimum and maximum values for the peak normalized particle kinetic energy are extracted to be 0.0282 and 0.0292, respectively. The difference between the two extreme values is about 3.5% of the mean value. Considering the fact that the variations of the normalized runout distance and the normalized peak particle kinetic energy when the initial column length  $L_i$  increases from 3 to 10 cm are as large as



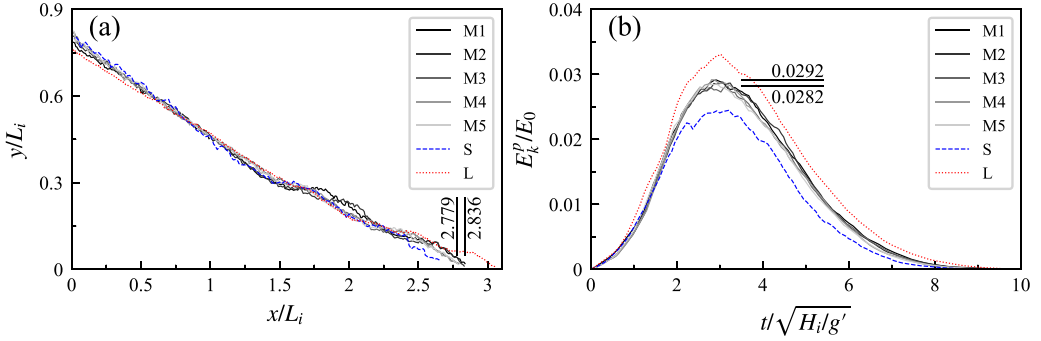


FIG. 17. Numerical results: comparison between the five repeated LBM-DEM simulations of underwater granular column collapse of a medium size with different random seeds ( $L_i = 5$  cm and denoted as M1, M2, M3, M4, and M5), together with the small (S:  $L_i = 3$  cm) and large (L:  $L_i = 10$  cm) cases, when the initial aspect ratio  $a = 1$  for (a) the final granular free-surface profile and (b) the particle kinetic energy evolution. The minimum and the maximum values of the normalized runout distance and the normalized peak particle kinetic energy from the five repeated simulations are indicated by the solid straight lines.

15.1% and 35.2%, respectively, we can conclude that the influence of random seed is much smaller compared to the column size effects.

- 
- [1] C. Cassar, M. Nicolas, and O. Pouliquen, Submarine granular flows down inclined planes, *Phys. Fluids* **17**, 103301 (2005).
  - [2] P. Jop, Y. Forterre, and O. Pouliquen, A constitutive law for dense granular flows, *Nature (London)* **441**, 727 (2006).
  - [3] F. Boyer, E. Guazzelli, and O. Pouliquen, Unifying Suspension and Granular Rheology, *Phys. Rev. Lett.* **107**, 188301 (2011).
  - [4] R. Delannay, A. Valance, A. Mangeney, O. Roche, and P. Richard, Granular and particle-laden flows: From laboratory experiments to field observations, *J. Phys. D* **50**, 053001 (2017).
  - [5] S. Courrech du Pont, P. Gondret, B. Perrin, and M. Rabaud, Granular Avalanches in Fluids, *Phys. Rev. Lett.* **90**, 044301 (2003).
  - [6] A. Bougouin and L. Lacaze, Granular collapse in a fluid: Different flow regimes for an initially dense-packing, *Phys. Rev. Fluids* **3**, 064305 (2018).
  - [7] E. Lajeunesse, J. B. Monnier, and G. M. Homsy, Granular slumping on a horizontal surface, *Phys. Fluids* **17**, 103302 (2005).
  - [8] G. Lube, H. E. Huppert, R. S. J. Sparks, and A. Freundt, Collapses of two-dimensional granular columns, *Phys. Rev. E* **72**, 041301 (2005).
  - [9] N. J. Balmforth and R. R. Kerswell, Granular collapse in two dimensions, *J. Fluid Mech.* **538**, 399 (2005).
  - [10] L. Staron and E. J. Hinch, Study of the collapse of granular columns using two-dimensional discrete-grain simulation, *J. Fluid Mech.* **545**, 1 (2005).
  - [11] L. Jing, G. C. Yang, C. Y. Kwok, and Y. D. Sobral, Dynamics and scaling laws of underwater granular collapse with varying aspect ratios, *Phys. Rev. E* **98**, 042901 (2018).
  - [12] E. L. Thompson and H. E. Huppert, Granular column collapses: Further experimental results, *J. Fluid Mech.* **575**, 177 (2007).
  - [13] V. Topin, Y. Monerie, F. Perales, and F. Radjaï, Collapse Dynamics and Runout of Dense Granular Materials in a Fluid, *Phys. Rev. Lett.* **109**, 188001 (2012).
  - [14] L. Jing, G. C. Yang, C. Y. Kwok, and Y. D. Sobral, Flow regimes and dynamic similarity of immersed granular collapse: A CFD-DEM investigation, *Powder Technol.* **345**, 532 (2019).

- [15] L. Rondon, O. Pouliquen, and P. Aussillous, Granular collapse in a fluid: Role of the initial volume fraction, *Phys. Fluids* **23**, 073301 (2011).
- [16] C. Wang, Y. Wang, C. Peng, and X. Meng, Dilatancy and compaction effects on the submerged granular column collapse, *Phys. Fluids* **29**, 103307 (2017).
- [17] E. Izard, L. Lacaze, T. Bonometti, and A. Pedrono, Numerical Modeling of a Granular Collapse Immersed in a Viscous Fluid, in *Advances in Hydroinformatics*, edited by P. Gourbesville, J. Cunge, and G. Caignaert (Springer, Singapore, 2018), pp. 1099–1116.
- [18] G. C. Yang, L. Jing, C. Y. Kwok, and Y. D. Sobral, Pore-scale simulation of immersed granular collapse: Implications to submarine landslides, *J. Geophys. Res.: Earth Surface* **125**, e2019JF005044 (2020).
- [19] R. M. Iverson, M. E. Reid, N. R. Iverson, R. G. LaHusen, M. Logan, J. E. Mann, and D. L. Brien, Acute sensitivity of landslide rates to initial soil porosity, *Science* **290**, 513 (2000).
- [20] C. H. Lee, Z. Huang, and M. L. Yu, Collapse of submerged granular columns in loose packing: Experiment and two-phase flow simulation, *Phys. Fluids* **30**, 123307 (2018).
- [21] A. C. Santomaso, S. Volpato, and F. Gabrieli, Collapse and runout of granular columns in pendular state, *Phys. Fluids* **30**, 063301 (2018).
- [22] A. Bougouin, L. Lacaze, and T. Bonometti, Collapse of a liquid-saturated granular column on a horizontal plane, *Phys. Rev. Fluids* **4**, 124306 (2019).
- [23] T. H. Eismann, Mechanisms of large landslides, *Rock Mech.* **12**, 15 (1979).
- [24] H. J. Melosh, Acoustic fluidization: A new geologic process? *J. Geophys. Res.: Solid Earth* **84**, 7513 (1979).
- [25] P. E. Kent, The transport mechanism in catastrophic rock falls, *J. Geol.* **74**, 79 (1966).
- [26] R. L. Shreve, Leakage and fluidization in air-layer lubricated avalanches, *GSA Bull.* **79**, 653 (1968).
- [27] D. Mohrig, C. Ellis, G. Parker, K. X. Whipple, and M. Hondzo, Hydroplaning of subaqueous debris flows, *GSA Bull.* **110**, 387 (1998).
- [28] J. M. Warnett, P. Denissenko, P. J. Thomas, E. Kiraci, and M. A. Williams, Scalings of axisymmetric granular column collapse, *Granular Matter* **16**, 115 (2014).
- [29] O. Pouliquen, Scaling laws in granular flows down rough inclined planes, *Phys. Fluids* **11**, 542 (1999).
- [30] R. M. Iverson and R. P. Denlinger, Flow of variably fluidized granular masses across three-dimensional terrain: 1. Coulomb mixture theory, *J. Geophys. Res.: Solid Earth* **106**, 537 (2001).
- [31] C. Meruane, A. Tamburrino, and O. Roche, On the role of the ambient fluid on gravitational granular flow dynamics, *J. Fluid Mech.* **648**, 381 (2010).
- [32] A. S. Baumgarten and K. Kamrin, A general fluid-sediment mixture model and constitutive theory validated in many flow regimes, *J. Fluid Mech.* **861**, 721 (2019).
- [33] G. C. Yang, L. Jing, C. Y. Kwok, and Y. D. Sobral, A comprehensive parametric study of LBM-DEM for immersed granular flows, *Comput. Geotech.* **114**, 103100 (2019).
- [34] G. Pinzon and M. Cabrera, Planar collapse of a submerged granular column, *Phys. Fluids* **31**, 086603 (2019).
- [35] G. C. Yang, C. Y. Kwok, and Y. D. Sobral, The effects of bed form roughness on total suspended load via the lattice Boltzmann method, *Appl. Math. Model.* **63**, 591 (2018).
- [36] L. Jing, C. Y. Kwok, Y. F. Leung, and Y. D. Sobral, Extended CFD-DEM for free-surface flow with multi-size granules, *Int. J. Numer. Anal. Methods Geomech.* **40**, 62 (2016).
- [37] D. R. Noble and J. R. Torczynski, A lattice-Boltzmann method for partially saturated computational cells, *Int. J. Mod. Phys. C* **09**, 1189 (1998).
- [38] P. L. Bhatnagar, E. P. Gross, and M. Krook, A model for collision processes in gases. I. Small amplitude processes in charged and neutral one-component systems, *Phys. Rev.* **94**, 511 (1954).
- [39] Y. H. Qian, D. D’Humières, and P. Lallemand, Lattice BGK models for Navier-Stokes equation, *Europhys. Lett.* **17**, 479 (1992).
- [40] X. He and L.-S. Luo, Theory of the lattice Boltzmann method: From the Boltzmann equation to the lattice Boltzmann equation, *Phys. Rev. E* **56**, 6811 (1997).
- [41] P. A. Cundall and O. D. L. Strack, A discrete numerical model for granular assemblies, *Géotechnique* **29**, 47 (1979).

- [42] A. Di Renzo and F. P. Di Maio, Comparison of contact-force models for the simulation of collisions in DEM-based granular flow codes, *Chem. Eng. Sci.* **59**, 525 (2004).
- [43] Q. Zou and X. He, On pressure and velocity boundary conditions for the lattice Boltzmann BGK model, *Phys. Fluids* **9**, 1591 (1997).
- [44] G. C. Yang, L. Jing, C. Y. Kwok, and Y. D. Sobral, A question of scaling in immersed granular collapses, in *2nd International Conference on the Material Point Method for Modelling Soil-Water-Structure Interaction* (China Ocean Press, Cambridge, UK, 2019), pp. 229–233.
- [45] L. Jing, C. Y. Kwok, Y. F. Leung, and Y. D. Sobral, Characterization of base roughness for granular chute flows, *Phys. Rev. E* **94**, 052901 (2016).
- [46] Q. Wang, R. Hosseini, and K. Kumar, Effect of initial volume on the run-out behavior of submerged granular columns, in *IFCEE 2021*, edited by C. El Mohtar, S. Kulesza, T. Baser, and M. D. Venezia (American Society of Civil Engineers, Dallas, Texas, 2021), pp. 256–265.
- [47] See Supplemental Material at <http://link.aps.org/supplemental/10.1103/PhysRevFluids.6.114302> for the Video recordings of underwater granular collapse experiments: (1) Small: aspect ratio  $a = 1.5$ , initial column length  $L_i = 3$  cm; (2) Medium: aspect ratio  $a = 1.5$ , initial column length  $L_i = 5$  cm; and (3) Large: aspect ratio  $a = 1.5$ , initial column length  $L_i = 10$  cm.
- [48] L. Lacaze, J. Bouteloup, B. Fry, and E. Izard, Immersed granular collapse: From viscous to free-fall unsteady granular flows, *J. Fluid Mech.* **912**, A15 (2021).
- [49] Y. D. Sobral, T. F. Oliveira, and F. R. Cunha, On the unsteady forces during the motion of a sedimenting particle, *Powder Technol.* **178**, 129 (2007).
- [50] L. Staron and E. Lajeunesse, Understanding how volume affects the mobility of dry debris flows, *Geophys. Res. Lett.* **36**, L12402 (2009).
- [51] L. Lacaze and R. R. Kerswell, Axisymmetric Granular Collapse: A Transient 3D Flow Test of Viscoplasticity, *Phys. Rev. Lett.* **102**, 108305 (2009).